Journal of Energy Chemistry 88 (2024) 446–460

Contents lists available at ScienceDirect

Journal of Energy Chemistry

journal homepage: www.elsevier.com/locate/jechem

http://www.journals.elsevier.com/journal-of-energy-chemistry/

Review

Review and prospects on the low-voltage $Na_2Ti_3O_7$ anode materials for sodium-ion batteries

Jun Dong [a], Yalong Jiang [b,*], Ruxing Wang [a], Qiulong Wei [c], Qinyou An [d,*], Xiaoxing Zhang [a,*]

[a] Hubei Key Laboratory for High-efficiency Utilization of Solar Energy and Operation Control of Energy Storage System, Hubei University of Technology, Wuhan 430068, Hubei, China
[b] State Key Laboratory of New Textile Materials and Advanced Processing Technologies, Wuhan Textile University, Wuhan 430200, Hubei, China
[c] Xiamen Key Laboratory of High-Performance Metals and Materials, College of Materials, Xiamen University, Xiamen 361005, Fujian, China
[d] State Key Laboratory of Advanced Technology for Materials Synthesis and Processing, Wuhan University of Technology, Wuhan 430070, Hubei, China

ARTICLE INFO

Article history:
Received 28 July 2023
Revised 16 September 2023
Accepted 17 September 2023
Available online 13 October 2023

Keywords:
Sodium-ion batteries
Low-voltage anode materials
$Na_2Ti_3O_7$
Electrochemical performances
Electrochemical mechanism

ABSTRACT

Due to its low cost and natural abundance of sodium, Na-ion batteries (NIBs) are promising candidates for large-scale energy storage systems. The development of ultralow voltage anode materials is of great significance in improving the energy density of NIBs. Low-voltage anode materials, however, are severely lacking in NIBs. Of all the reported insertion oxides anodes, the $Na_2Ti_3O_7$ has the lowest operating voltage (an average potential of 0.3 V vs. Na^+/Na) and is less likely to deposit sodium, which has excellent potential for achieving NIBs with high energy densities and high safety. Although significant progress has been made, achieving $Na_2Ti_3O_7$ electrodes with excellent performance remains a severe challenge. This paper systematically summarizes and discusses the physicochemical properties and synthesis methods of $Na_2Ti_3O_7$. Then, the sodium storage mechanisms, key issues and challenges, and the optimization strategies for the electrochemical performance of $Na_2Ti_3O_7$ are classified and further elaborated. Finally, remaining challenges and future research directions on the $Na_2Ti_3O_7$ anode are highlighted. This review offers insights into the design of high-energy and high-safety NIBs.
© 2023 Science Press and Dalian Institute of Chemical Physics, Chinese Academy of Sciences. Published by ELSEVIER B.V. and Science Press. All rights reserved.



Jun Dong got her Ph.D. from the Wuhan University of Technology under the guidance of Professor Liqiang Mai. She currently works at the Hubei University of Technology. Her research interests focus on high-performance sodium-ion batteries for energy storage, especially electrode materials' performance optimization and electrochemical mechanism research.



Yalong Jiang is a lecturer at the State Key Laboratory of New Textile Materials and Advanced Processing Technologies, Wuhan Textile University. He received Ph.D. from the State Key Laboratory of Advanced Technology for Materials Synthesis and Processing, Wuhan University of Technology (WUT) in 2020, under the supervision of Prof. Liqiang Mai. He carried out his postdoctoral research in the laboratory of Prof. Liqiang Mai at WUT in 2021-2023. His research interests include energy storage materials and devices.

* Corresponding authors.
E-mail addresses: yljiang@wtu.edu.cn (Y. Jiang), anqinyou86@whut.edu.cn (Q. An), xiaoxing.zhang@outlook.com (X. Zhang).

https://doi.org/10.1016/j.jechem.2023.09.039
2095-4956/© 2023 Science Press and Dalian Institute of Chemical Physics, Chinese Academy of Sciences. Published by ELSEVIER B.V. and Science Press. All rights reserved.



Ruxing Wang received his Ph.D. in Materials Science from Huazhong University of Science and Technology, China in 2017. And then he worked as a post-doc researcher in Huazhong University of Science and Technology from 2017 to 2021. He currently works at Hubei University of Technology. His research interests mainly focus on energy storage technologies and new energy materials.



Qiulong Wei is currently an associate professor in the Department of Materials Science and Engineering of Xiamen University. He received his Ph.D. from Wuhan University of Technology in 2016, which was followed by postdoctoral experience under the guidance of Prof. Bruce Dunn at UCLA. His current research interests focus on the design and synthesis of active materials for electrochemical energy storage devices with both high energy density and power density.



Qinyou An is Professor at the State Key Laboratory of Advanced Technology for Materials Synthesis and Processing, Wuhan University of Technology (WUT). He received Ph.D. from WUT in 2014. He carried out his postdoctoral research in the laboratory of Prof. Yan Yao at the University of Houston in 2014-2015. Currently, his research interests include energy storage materials and devices.



Xiaoxing Zhang received a Ph.D. degree from Chongqing University. He was awarded as the Changjiang Scholar in 2020. He is a professor at School of Electrical and Electronic Engineering, Hubei University of Technology. His research interests are in the broad area of Smart Grid technologies, especially large-scale energy storage, online monitoring and fault diagnosis of high voltage electrical insulation equipment, eco-friendly gas insulating medium, and gas sensors.

1. Introduction

Rechargeable battery technology is one of the most promising renewable energy storage technologies to achieve a greener planet. Relatively advanced Li-ion batteries (LIBs) are widely used in various energy storage systems, and market demand for LIBs is overgrowing [1,2]. Lithium, on the other hand, is a non-abundant and unevenly distributed element in the crust of Earth, which has led to a significant increase in the prices of lithium-containing salts such as Li_2CO_3. Lithium supplies would further constrain the increasing expansion of LIB applications. Therefore, exploring new battery systems is highly meaningful [3–6]. In contrast to lithium, sodium is one of the most abundant elements in the Earth's crust [7]. Meanwhile, because of the similar assembly process, NIBs can utilize the manufacturing lines for LIBs, further reducing the costs [8]. Thus, NIBs show a strong attraction in large-scale energy storage systems, which can be an important complementary technology to LIBs [9,10]. Compared to well-developed LIBs, however, the electrochemical performance of NIBs is relatively inferior owing to the large radius of Na^+ (1.02 Å vs. 0.76 of Li^+), relatively higher standard electrode potential of Na^+/Na (−2.71 V vs. SHE) than that of Li^+/Li (−3.01 V vs. SHE), further restricting its applications in the market. Therefore, it is significant to develop NIBs with high energy and power density, long cycling life, cost-competitiveness, and safety [8,9].

One of conspicuous challenges in NIBs research is to search for appropriate anode materials. Ideal anode materials are expected to have a high capacity, superior rate capability, low potential, high safety, and long lifetime. Although various materials in terms of capacity and voltage can potentially be used as anodes, very few anodes are promising for commercial applications (Fig. 1) [11,12]. Hard carbon exhibits better sodium storage properties, but its low potential discharge plateau between 0 and 0.1 V vs. Na^+/Na may be more inclined to form the sodium dendrites and further raise safety concerns [13]. Of all other representative anode materials, titanium-based electrode materials are essential research objects in NIBs. Titanium-based electrode materials mainly include TiO_2, Na-Ti-O compounds, and Ti-based phosphates [7,12,14–16]. They exhibit appropriate operating voltage, low strain expansion, environmental friendliness, safety, and low costs [17–24]. Fig. 1(b) summarizes their intercalation potential, specific capacity, and energy density [12]. Most titanium-based electrode materials are typically endowed with an intercalation potential of 0.5–1 V vs. Na^+/Na, giving rise to a relatively narrow output voltage and a low energy density for full NIBs. In particular, the $Na_2Ti_3O_7$ exhibits the lowest intercalation potential (0.3 V vs. Na^+/Na) and the highest specific capacity among other reported titanium-based electrode materials. More importantly, the average potential of 0.3 V vs. Na^+/Na about $Na_2Ti_3O_7$ anode is almost the lowest for NIBs anodes, not only in oxides anodes but also among other reported candidate materials (Fig. 1a) [12]. A plateau with this voltage can be quite advantageous in terms of the energy density, when compared to other electrode materials of high potential such as $Na_3V_2(PO_4)_3$ (1.6 V), Na_xVO_2 (1.75 V), Ni_3S_2(0.94 V), or $NaTi_2(PO_4)_3$ (2.1 V) [25–27]. Due to the low intercalation potential of $Na_2Ti_3O_7$, the output voltage would be relatively higher, contributing to higher energy [11]. The plateau of $Na_2Ti_3O_7$ is also compared favorably with respect to hard carbon, since the possibility of sodium plating is reduced, due to its higher discharge plateau of 0.2 V vs. Na^+/Na [25]. Moreover, the calcination temperature of producing $Na_2Ti_3O_7$ is generally 800 °C, which is much lower than that of synthesizing hard carbon materials (between 1000 and 1600 °C). The energy consumption will be much lower after achieving industrial-scale production, which is greatly favorable to the commercialization of NIBs. Besides, $Na_2Ti_3O_7$ consists of zigzag layers of titanium-oxygen octahedral with sodium ions in the interlayer space that favors the storage of sodium ions. The essential advantages mentioned above are also summarized in Fig. 2. Therefore, $Na_2Ti_3O_7$ anode materials show excellent prospects for developing NIBs with high energy density and high safety.

As an anode essential for promoting the development of NIBs, the basic properties, synthetic mechanism, electrochemical properties, and outlook of the $Na_2Ti_3O_7$ anode materials should be fully captured. Therefore, the $Na_2Ti_3O_7$ materials are comprehensively reviewed (Fig. 2). The review would provide essential knowledge for further developing commercial $Na_2Ti_3O_7$ anodes and is organized as follows.

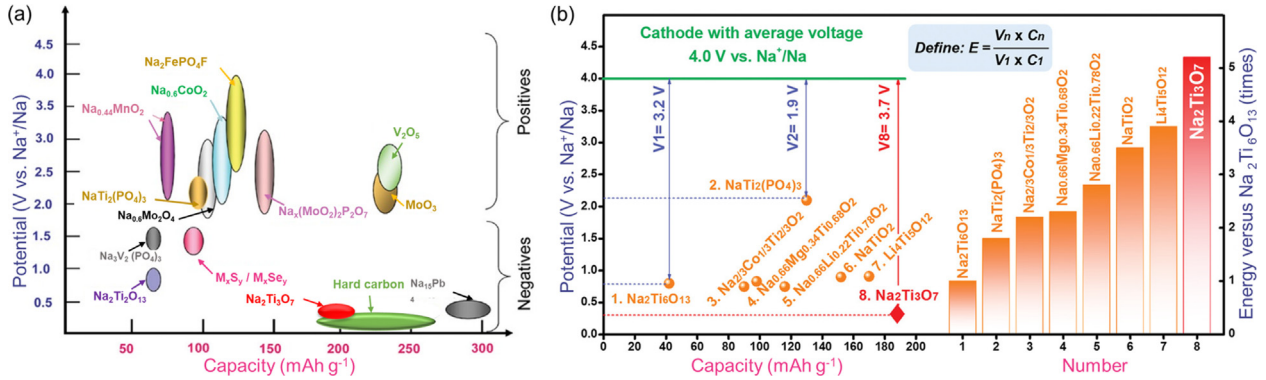


Fig. 1. Summary of the electrochemical performance of some representative electrode materials for NIBs. (a) Potential versus capacity plot. Reproduced with permission from Ref. [11]. Copyright 2011, American Chemical Society. (b) The comparison of $Na_2Ti_3O_7$ with titanium-based anodes in terms of intercalation potential, specific capacity, and energy density. Reproduced with permission from Ref. [12]. Copyright 2020, Wiley-VCH.

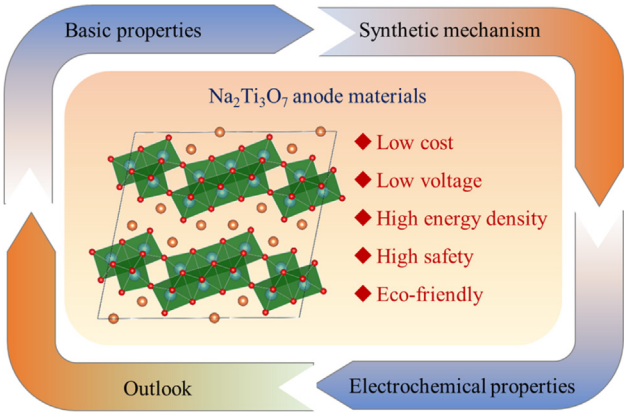


Fig. 2. The advantages of $Na_2Ti_3O_7$ anode materials and the organization of the review.

(1) Section 1 briefly introduces the development and advantages of $Na_2Ti_3O_7$ anodes. Section 2 gives a detailed description of the crystal structure and physicochemical properties of $Na_2Ti_3O_7$.
(2) Section 3 classifies and discusses the different synthetic methods of $Na_2Ti_3O_7$.
(3) Section 4 summarizes and discusses the electrochemical reaction mechanisms, key issues and challenges, optimization strategies, and applications of $Na_2Ti_3O_7$ in sodium-ion full cells.
(4) This review provides a summary and outlook on the $Na_2Ti_3O_7$ anodes for NIBs.

2. The crystal structure, physical and chemical properties of $Na_2Ti_3O_7$

2.1. The crystal structure of $Na_2Ti_3O_7$

Research on $Na_2Ti_3O_7$ was started in 1961. Andersson and Wadsley determined that the layered crystal structure of $Na_2Ti_3O_7$ is monoclinic, and the space group is $P2_1/m$ [28]. Yakubovich and Kireev refined the lattice parameters of monoclinic, i.e., a = 9.133(2), b = 3.806(1), c = 8.566(2), and β = 101.57°(3°), and the coordinates of the basis atoms and equivalent thermal parameters are detailed (Table S1) [29]. The above-detailed coordinates parameters make the three-dimensional arrangement of atoms in $Na_2Ti_3O_7$ explicit, as shown by crystal structure models in Fig. 3(a and b) [30]. The

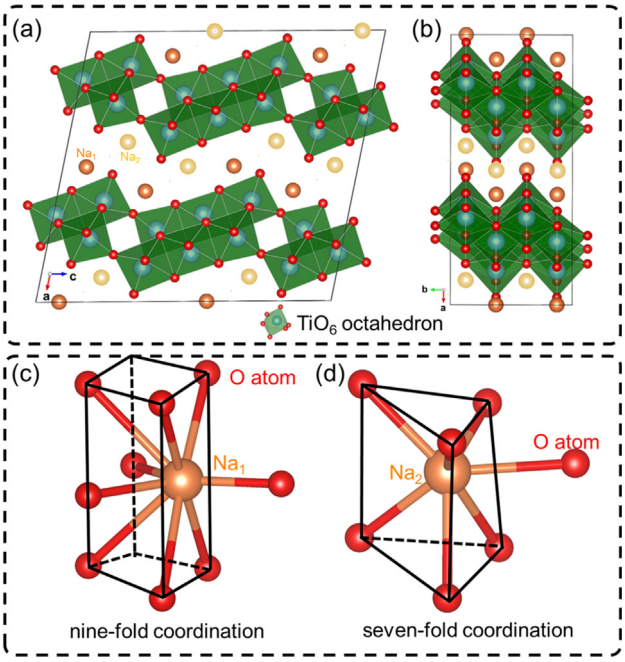


Fig. 3. (a, b) Monoclinic $Na_2Ti_3O_7$ unit cell with $P2_1/m$ space group viewed along the b and c axes, respectively. (c, d) The nine-fold coordination of Na_1 and the seven-fold coordination of Na_2, respectively.

basic unit of each layer is a block of six distorted TiO_6 octahedral. Three of them (named as $(Ti_3O_7)^{2-}$ unit) are at one level by sharing their edges and simultaneously linked with the other three by sharing corners at a distance b/2 Å above or below (Fig. 3a). Sodium ions occupy two crystallographic sites (Na_1 and Na_2) and hold the layers together. The Na_1–O presents an irregular nine-coordination, like a cube (Fig. 3c). In particular, two oxygen atoms at one edge are replaced by one oxygen at the center of the same edge, and two additional oxygen atoms are on the outside of opposite faces. The Na_2–O shows the seven-coordination (Fig. 3d), like a trigonal prism, and the seventh oxygen is on the outside of a face. In addition, a new triclinic phase $Na_2Ti_3O_7$ is reported by Li et al. [12]. The space group of triclinic phase $Na_2Ti_3O_7$ is P-1, with the lattice parameters a = 9.1332 Å, b = 3.8041 Å, c = 8.5663 Å, and $\alpha \neq \gamma \neq 90°$ and β = 101.6°, different from the monoclinic phase ($\alpha = \gamma = 90°$) [12]. The layer spacing of the triclinic phase is 8.5663 Å, and the bond length between O3 and O6 atoms is 4.61 Å, which is smaller than that of the monoclinic phase. It visually distinguished the two phases based on the peak intensity ratio

of I_{100}/I_{104}. The ratio values are 3.6 and 1.48 for the triclinic and monoclinic phases, respectively.

The ion doping could regulate the crystal structure. As for $Na_2Ti_3O_7$, the H^+/Na^+ cation-exchange process could lead to the formation of $H_2Ti_3O_7$. The H^+ position can be classified into three types, and the $(Ti_3O_7)^{2-}$ layers would glide with a space group of $C2/m$ [31]. For the low percentage of manganese doping, Mn^{3+} ions would substitute the partial Ti^{4+} sites, while Mn^{2+} ions would occupy the partial Na^+ sites. In addition, the Mn^{3+} substitution at the Ti^{4+} sites will dilate interlayer space, but the Mn^{2+} substitution at the Na^+ sites will lead to the contraction of interlayer space [32]. A similar phenomenon is also observed for Fe-doping $Na_2Ti_3O_7$ [32]. Besides, the Li^+-doping in the interlayer of $Na_2Ti_3O_7$ will reduce Ti^{4+} ions to Ti^{3+} and expand interlayer space [33].

2.2. Physical and chemical properties

The fundamental physical property of $Na_2Ti_3O_7$ was systematically discovered through experiments and theoretical calculations [32,34,35]. Among them, the conductive properties of $Na_2Ti_3O_7$ are closely related to their electrochemical performance, which can be assessed across band gaps. The $Na_2Ti_3O_7$ is a semiconductor with an indirect gap of 2.99 eV based on density functional theory (DFT) [34]. Araújo-Filho et al. found that the charge transport of $Na_2Ti_3O_7$ would be dominated by holes [30]. Besides, the primary energy band gap was estimated to be 3.51 eV by an ultraviolet and visible (UV–Vis) spectroscopy experiment (Fig. 4a) [30]. However, pure DFT methods are unable to reproduce the main gap in solids, with errors typically larger than 40% for insulators and semiconductors using the local density approximation (LDA) exchange-correlation energy, so more advanced methods (ab initio GW approximation based on Green's function, hybrid functions, the random-phase approximation, and screened exchange LDA) must be applied to refine [30]. Besides, $Na_2Ti_3O_7$ shows electronic-hopping conduction involving the loose electrons of $(Ti_3O_7)^{2-}$ in the temperature range of 370–415 K [32]. Kikkawa and Koizumi discovered that the ionic conduction of $Na_2Ti_3O_7$ will become prominent at higher temperatures [32,36]. Scanlon et al. found that intrinsic defects of $Na_2Ti_3O_7$ impair electrical conductivity [37]. It was found that the insulating properties of $Na_2Ti_3O_7$ arise from the Na and O Schottky disorder that act as major charge compensators. The conductivity of $Na_2Ti_3O_7$ would be optimized by ion doping and vacancy defects [32,36,37]. For example, substituting partial Ti^{4+} with Mn^{3+} would naturally increase the number of loose electrons, increasing conductivity [32]. The $Na_{2-x}Li_xTi_3O_7$ synthesized by substituting partial Na^+ with Li^+ shows electron-hopping conduction, and the conductivity increases as the concentration of lithium increases [33]. The Na and O vacancies in $Na_2Ti_3O_7$ may also enhance electrical conductivity [37].

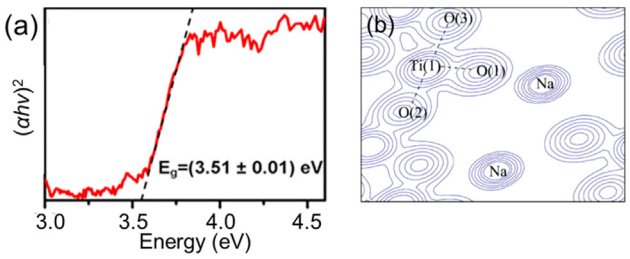


Fig. 4. (a) Squared measured optical absorption in the 3.0–4.5 eV range. Reproduced with permission from Ref. [30]. Copyright 2017, Elsevier. (b) The electron density map on the (040) plane of $Na_2Ti_3O_7$ (contour lines are drawn at 3 electrons $Å^{-3}$ intervals). Reproduced with permission from Ref. [34]. Copyright 2011, Springer.

The other critical property of $Na_2Ti_3O_7$ is the ion-exchange characteristic. The $Na_2Ti_3O_7$ consists of ionic and covalent bonds, as shown in the electron density map (Fig. 4b) [34]. The covalent bond depends on a strong interaction between the Ti 3*d* and O 2*p* orbitals, which helps to stabilize the $(Ti_3O_7)^{2-}$ layers. The interlayer structure is stable due to the ionic bonding between the Na^+ and $(Ti_3O_7)^{2-}$ layers. The $Na_2Ti_3O_7$ is favorable for the ion exchange process because of the ionic bonds. Na^+ can be exchanged with alkylammonium ions, leading to an expansion of interlayer space [28]. The ion exchange process between Na^+ and H^+ occurs in a wide range of pH, from acidic solutions to highly concentrated alkaline aqueous solutions [38]. $Na_{1.5}H_{0.5}Ti_3O_7$ and $H_2Ti_3O_7$ would be respectively obtained by exchange process in the pH = 13 and pH = 1 solutions. Thus, the pure phase of $Na_2Ti_3O_7$ throughout the preparation process should avoid water. Ion-exchange characteristic of $Na_2Ti_3O_7$ could be widely applied to the exfoliation of layer structure [39] and the preparation of other compounds (for example $H_2Ti_3O_7$ [31,35], Ag^+-$H_2Ti_3O_7$ [40], $Li_2Ti_3O_7$ [41], propylammonium/Ti_3O_7 [39], $CuTi_3O_7$ [42], and $Ag_2Ti_3O_7$ [42]).

3. Synthetic methods of $Na_2Ti_3O_7$

3.1. Solid-state sintering method

The solid-state sintering method is simple and cost-effective, which is widely applied to synthesize $Na_2Ti_3O_7$ materials [12,25,28,32,35,40,43–46]. The reasonable solid-state sintering conditions are the key to obtaining a pure $Na_2Ti_3O_7$ phase. This section reviews the key synthesized conditions, including the type and molar ratio of precursors, the temperature, time and number of calcinations, and the cooling atmosphere. The related research progress and achievements of solid-state sintering conditions to obtain pure $Na_2Ti_3O_7$ phase are summarized in Fig. 5. The solid-state sintering methods are summarized in Table S2.

Mahmoud et al. clearly described the formation mechanism and process of $Na_2Ti_3O_7$ including three steps [47]. Firstly, the $Na_4Ti_5O_{12}$ phase begins to form at ~540 °C; then, the $Na_2Ti_6O_{13}$ phase appears as the remaining TiO_2 reacts with the part of the $Na_4Ti_5O_{12}$ at ~700 °C; finally, the two phases of $Na_4Ti_5O_{12}$ and $Na_2Ti_6O_{13}$ react at 800 °C to form $Na_2Ti_3O_7$. As for precursors, TiO_2 is found to be widely used as a titanium precursor, but the sodium precursors are various, including Na_2CO_3, NaOH, and CH_3COONa (Fig. 5). With different particle sizes of TiO_2 precursor and types of sodium precursors, the required calcination time and temperature for synthesizing pure phase are different. In order to establish the factors that govern the formation of pure $Na_2Ti_3O_7$, Balaya et al. studied the effects of calcination temperature and time on two different sodium precursors [35]. Using NaOH as the sodium precursor, the $Na_2Ti_3O_7$ phase would be obtained at the calcination temperature of 750 °C. At the same temperature, the calcination time from 20 to 40 h does not change the purity of the phase. The calcination temperature is further increased to 850 °C, the impurities of $Na_2Ti_6O_{13}$ and the content of rutile TiO_2 increase, which would further increase after a longer calcination time. In particular, when the sodium precursor is NaOH in place of Na_2CO_3, there is no residual unreacted precursor in the sample [44]. When sodium acetate (CH_3COONa) is used as the sodium precursor, the pure phase is obtained at a higher temperature of 850 °C. Interestingly, the purity of $Na_2Ti_3O_7$ increases as the calcination time is extended, which is opposite to that observed in the NaOH precursor [25]. Besides, Lu et al. found that small-sized TiO_2 contributed to the synthesis of small-sized $Na_2Ti_3O_7$ because smaller-sized reactants would cause a higher reaction rate that could form a huge amount of crystalline nuclei in a short time and inhibit crystal growth [40]. Thus,

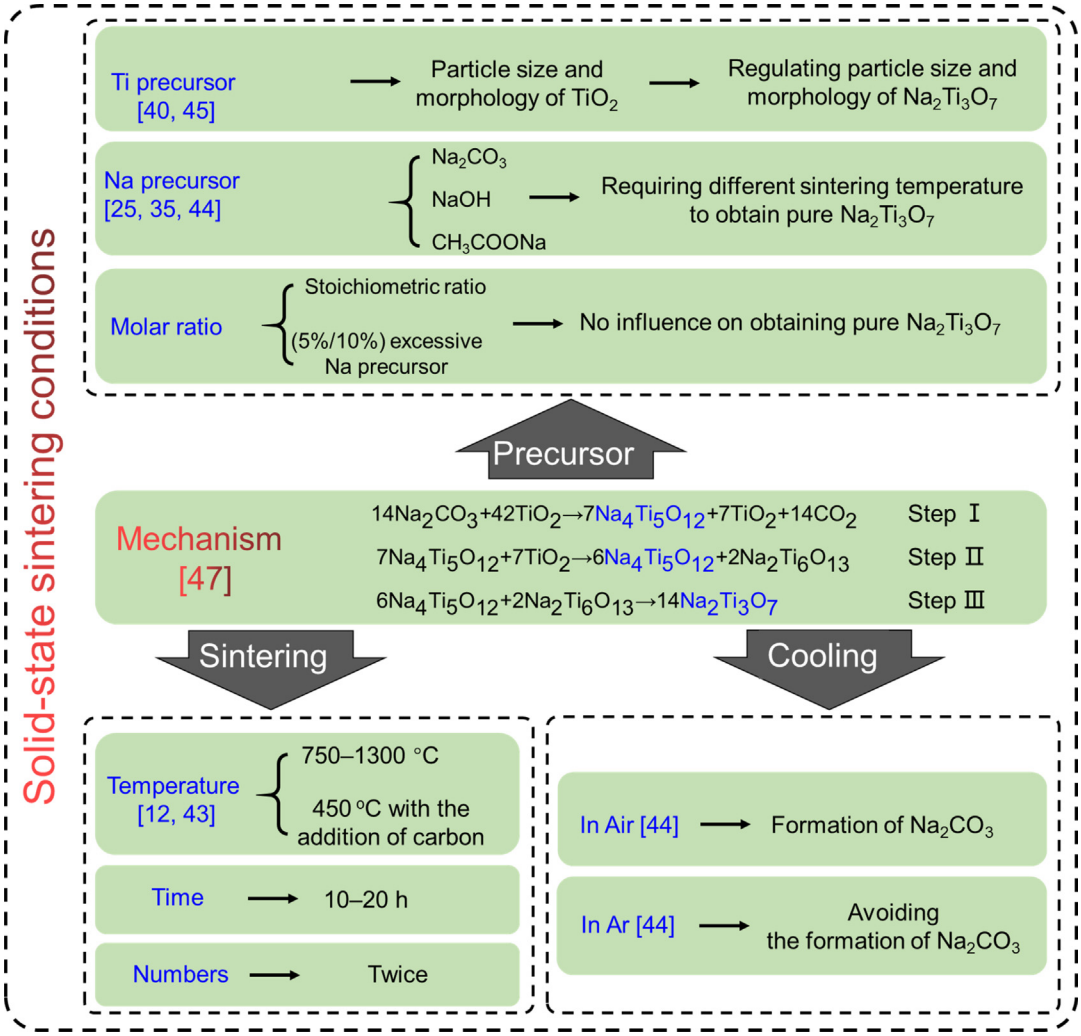


Fig. 5. The research progress and achievements of solid-state sintering conditions to obtain pure $Na_2Ti_3O_7$ phase.

smaller-sized $Na_2Ti_3O_7$ could be obtained at 800 °C by reacting for 8 h using 20 nm TiO_2. However, the calcination time would extend to 16 or 40 h, and the particle size of $Na_2Ti_3O_7$ would increase. Besides, the TiO_2 morphology can regulate the morphology of synthesized $Na_2Ti_3O_7$. The synthesized $Na_2Ti_3O_7$ morphology is usually micro-particles. Using hollow sphere TiO_2 as a titanium source, sheet-like $Na_2Ti_3O_7$ was synthesized instead [45]. The molar ratio of titanium and sodium precursors could be determined by the ratio of stoichiometric. Sodium precursors with either 5% or 10% excessive contents have no effect on obtaining the pure $Na_2Ti_3O_7$ phase. Thus, whether the Na precursor is excessive is not critical in obtaining a pure $Na_2Ti_3O_7$ phase.

The solid-state sintering temperature is vital in obtaining the pure $Na_2Ti_3O_7$ phase, which is usually between 750 to 1300 °C, as summarized in Fig. 5. Especially, Li et al. found that adding carbon could decrease the sintering temperature to 450 °C, much lower than conventional solid-state sintering methods [43]. Li et al. found that the monoclinic phase would be transformed into triclinic $Na_2Ti_3O_7$ by increasing the solid-state sintering temperature from 800 to 1000 °C [12]. In the following cooling process, the cooling atmosphere plays a critical role in obtaining pure $Na_2Ti_3O_7$ phase. Casas-Cabanas et al. found that it would form passivated Na_2CO_3 when cooling in the air, but it does not exist upon cooling in the Ar atmosphere (Fig. 5) [44]. Moreover, phthalocyanine or glucose is usually used as a carbon source for preparing carbon-coating $Na_2Ti_3O_7$ [44,46].

3.2. The synthetic methods of $Na_2Ti_3O_7$ with different morphology

As mentioned in the previous section, the solid-state sintering method is widely applied to synthesize $Na_2Ti_3O_7$. Through the solid-state sintering method, the synthesized $Na_2Ti_3O_7$ morphology is usually micro/nano-particles. Different synthetic methods could obtain different dimensional morphology. This section reviews the synthetic methods of $Na_2Ti_3O_7$ nanomaterials with one-dimensional (1D), two-dimensional (2D), and three-dimensional (3D) morphology.

1D $Na_2Ti_3O_7$ materials offer a short electron/ion transport pathway, conducive to high-rate applications. Solvothermal and hydrothermal methods are very effective for synthesizing 1D $Na_2Ti_3O_7$ nanomaterials using different solvents [48–50]. For successfully preparing 1D $Na_2Ti_3O_7$ nanomaterials, the solvents are usually ethanol or alkaline solution. Tang et al. synthesized the 1D $Na_2Ti_3O_7$ nanowires homogeneously embedded into reduced graphene oxide ($Na_2Ti_3O_7$/rGO) via a facile solvothermal method in the ethanol solution, showing a porous spider web-like network (Fig. 6a) [48]. The nanowires are 70–110 nm in diameter and 5–20 μm in length. The porous spider web-like morphology provides

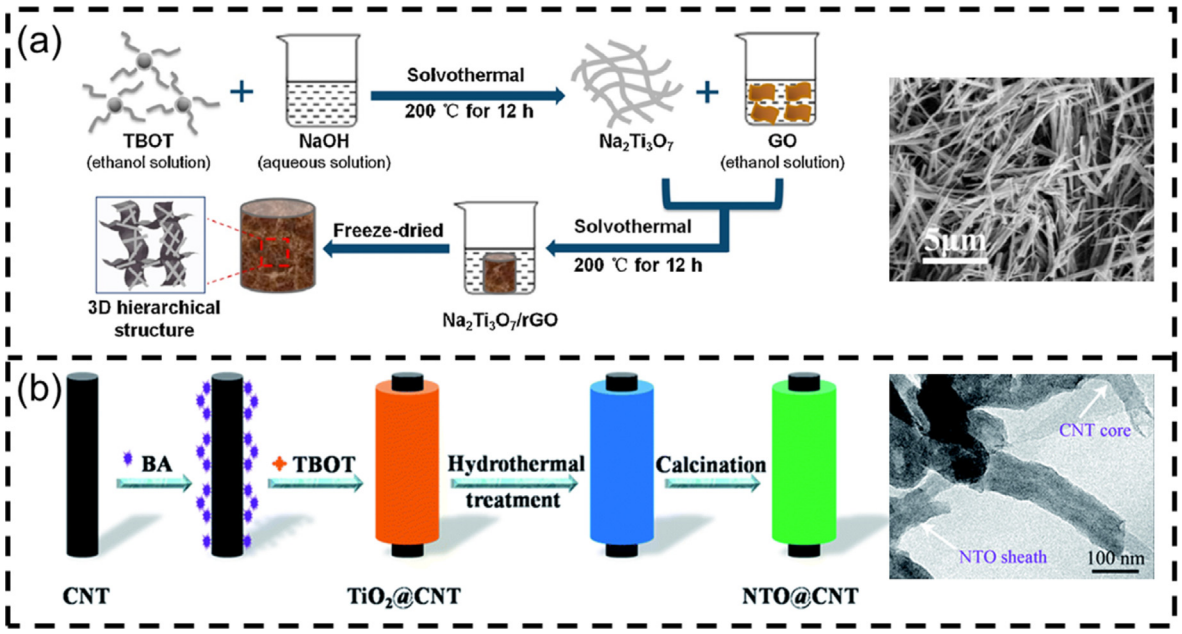


Fig. 6. The morphology of 1D $Na_2Ti_3O_7$. (a) Synthetic schematic illustration and morphology images of $Na_2Ti_3O_7$/rGO. Reproduced with permission from Ref. [48]. Copyright 2016, Elsevier. (b) Synthetic schematic illustration and morphology images of $Na_2Ti_3O_7$@CNT coaxial nanocables. Reproduced with permission from Ref. [51]. Copyright 2015, Royal Society of Chemistry.

an ideal conductive matrix for rapid electron/ion transportation. Yu et al. prepared $Na_2Ti_3O_7$ nanotubes under alkaline conditions with a diameter of approximately 10 nm [49]. Another universal method for preparing 1D nanomaterials is using 1D models, for example, carbon nanotubes (CNTs), followed by annealing treatment. Zhang et al. used 1D CNTs as a model and grew $Na_2Ti_3O_7$ on 1D CNTs. Using a sol–gel method and subsequent in-situ chemical sodiation and short calcination, they successfully fabricated 1D $Na_2Ti_3O_7$@CNT coaxial nano cables. The $Na_2Ti_3O_7$ layer is uniformly grown on CNTs with a thickness of about 25 nm (Fig. 6b) [51]. There exist many open mesopores at the tip of $Na_2Ti_3O_7$@CNT coaxial nanocables. A summary of main synthesis methods for 1D $Na_2Ti_3O_7$ is shown in Table S3.

The 2D $Na_2Ti_3O_7$ could be prepared by alkaline hydrothermal method [38], continuous hydrothermal flow synthesis route [52], and liquid-phase exfoliation method [39,53]. Through the alkaline hydrothermal method, the $Na_2Ti_3O_7$ nanosheet thin films exhibit widths of 100 nm, lengths of about 1 μm, and a thickness of about 2 nm at the molecular level (Fig. 7a) [38]. Based on a novel continuous hydrothermal flow system, extensive ultra-thin 2D $Na_2Ti_3O_7$ nanosheets are synthesized using a superheated water flow at 450 °C and 24.1 MPa as a crystallizing medium [52]. The as-prepared material consists of extensive and flat (2D) loosely stacked thin sheets with a size of ca. 400 nm × 400 nm (Fig. 7b). Liquid-phase exfoliation methods could also be used to synthesize $Na_2Ti_3O_7$ nanosheets. The layered structure of $Na_2Ti_3O_7$ could be exfoliated by intercalating large cations to swell the interlayers. Based on the above methods, the transparent propylammonium/Ti_3O_7 (PA/Ti_3O_7) films with a thickness of about 1 μm are obtained (Fig. 7c) [39]. Subsequently, Dunn et al. synthesized $Na_2Ti_3O_7$ nanoplatelets ($Na_2Ti_3O_7$ NP) and nanosheets (PA/Ti_3O_7 NS) by varying the centrifugation speed based on the above methods [53]. PA/Ti_3O_7 NS appears to be almost transparent, with a sheet thickness of about 1.2 nm (Fig. 7d). When the $Na_2Ti_3O_7$ NP is obtained within a transparent PA/Ti_3O_7 NS bed, widths range from 100 to 200 nm, with lengths ranging from several hundred nanometers to micrometers (Fig. 7d). The liquid-phase exfoliation method includes proton exchange, intercalation of large cations, and exfoliation (Fig. 7e). A summary of main synthesis methods for 2D $Na_2Ti_3O_7$ is shown in Table S4.

The reported 3D $Na_2Ti_3O_7$ includes a microsphere, micro flowers, red blood cell-like structure, and nanotube arrays. The corresponding synthetic methods mainly involve spray-drying methods, solvothermal approach methods, and hydrothermal methods. The $Na_2Ti_3O_7$ microsphere is synthesized by spray drying and solid-state calcination [54]. The spray-dried precursors consist of microspheres with an average diameter of 3–5 μm. The spherical shape can be well retained while the sintering period is short, i.e., 5 h, regardless of the temperature ranging from 700 to 800 °C, but not at 800 °C for 10 h (Fig. 8a) [54]. A novel flower-like architecture $Na_2Ti_3O_7$ was successfully synthesized. The $Na_2Ti_3O_7$ microflowers show a diameter ranging from 1 to 2 μm and consist of 5 nm thin nanosheets (Fig. 8b) [55]. A unique red blood cell-like hollow carbon sphere-supported $Na_2Ti_3O_7$ nanosheet structure ($Na_2Ti_3O_7$@-RHCS) was designed, exhibiting compact arrangements of nanosheets. Moreover, the thickness of the $Na_2Ti_3O_7$ nanosheets' shell is around 80 nm (Fig. 8c and d) [56]. The arrays of $Na_2Ti_3O_7$ nanosheet are uniformly grown on carbon textiles by hydrothermal reaction, presenting terrific flexibility, and the nanosheet shows a width of ca. 100 nm and length of ca. 1 μm [57]. The arrays of $Na_2Ti_3O_7$ nanotube supported on flexible Ti substrates are synthesized by hydrothermal methods. The nanotubes exhibit a core–shell structure consisting of a crystalline core and disordered shell and have an average longitudinal length of ca. 3 μm, inner diameters of 5 nm, and external diameters of 25–35 nm, respectively [58]. A summary of main synthesis methods for 3D $Na_2Ti_3O_7$ is shown in Table S5.

Overall, $Na_2Ti_3O_7$ with different dimensional morphology requires the selection of different synthesis methods. Solid-phase sintering is more economical and suitable for large-scale synthesis, but most of the products have the morphology of micro particles or nanorods. Compared with solid-phase sintering, the liquid-phase method is easier to modulate the $Na_2Ti_3O_7$ morphology. From the summary in Tables S2–S5, it can be seen that the solid-phase sintering method is simple and usually includes fewer than 4 synthesis steps, while the synthesis methods used to synthesize 1D, 2D,

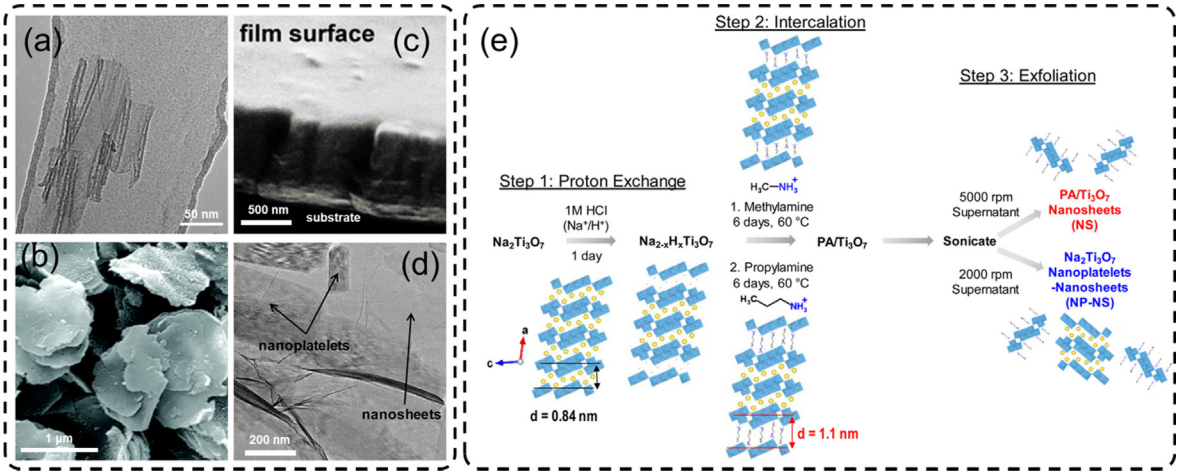


Fig. 7. The morphology of 2D $Na_2Ti_3O_7$. (a) TEM image of $Na_2Ti_3O_7$ nanosheet thin film. Reproduced with permission from Ref. [38]. Copyright 2014, Elsevier. (b) SEM images of ultra-thin 2D $Na_2Ti_3O_7$ nanosheets based on continuous hydrothermal flow system. Reproduced with permission from Ref. [52]. Copyright 2010, Royal Society of Chemistry. (c) SEM image of a PA/Ti_3O_7 film formed on glass substrate. Reproduced with permission from Ref. [39]. Copyright 2004, Royal Society of Chemistry. (d) Mixed nanoplatelets and nanosheets of $Na_2Ti_3O_7$ and (e) the liquid-phase exfoliation flowchart. Reproduced with permission from Ref. [53]. Copyright 2016, American Chemical Society.

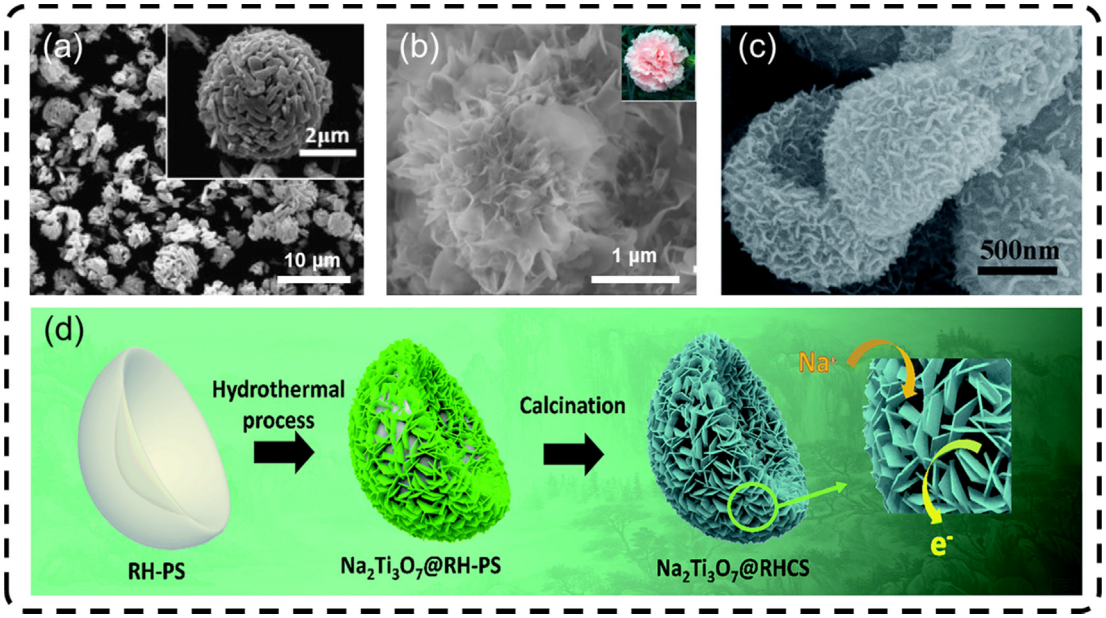


Fig. 8. The morphology of 3D $Na_2Ti_3O_7$. (a) SEM images of $Na_2Ti_3O_7$ by spray drying at 800 °C. Reproduced with permission from Ref. [54]. Copyright 2014, Elsevier. (b) SEM images of $Na_2Ti_3O_7$ microflowers. Reproduced with permission from Ref. [55]. Copyright 2017, American Chemical Society. (c, d) The morphology images and synthetic schematic illustration of $Na_2Ti_3O_7$@RHCS. Reproduced with permission from Ref. [56]. Copyright 2018, Royal Society of Chemistry.

and 3D structure need more steps, and some of them are even up to 8 steps.

4. $Na_2Ti_3O_7$ anodes for sodium-ion storage

4.1. Electrochemical reaction mechanism of $Na_2Ti_3O_7$ anodes

The electrochemical reaction mechanism of $Na_2Ti_3O_7$ anodes is summarized in Fig. 9. As seen from the voltage versus composition profile for the $Na_2Ti_3O_7$ [11], the $Na_2Ti_3O_7$ anode can reversibly insert $2Na^+$ per formula unit in the voltage range of 0.01–2.5 V vs. Na^+/Na, corresponding to a theoretical capacity of 177 mA h g^{-1} and a reduction of 2/3 of Ti^{4+} to Ti^{3+} ions. The irreversible electrochemical process around 0.7 V vs. Na^+/Na corresponds to the reaction of carbon black (conductive additive). The Na^+ ions mainly favorably travel along the layers (Path 1), and rarely diffuse through the layers (Path 2), and the Na^+ diffusion coefficient for Na^+ insertion is approximately 3.48×10^{-12} cm^2 s^{-1} [25,59]. The phase transformation mechanism of $Na_2Ti_3O_7$ after full discharge was proposed. Most views believe that the complete intercalated phase was $Na_4Ti_3O_7$. Palacín et al. proposed the structural models for the $Na_{2+x}Ti_3O_7$ based on density functional theory (DFT) calculations and experimental data [60]. After inserting the two additional Na^+ (forming $Na_4Ti_3O_7$ phase), the Na sublattice would rearrange, and the Na^+ ions in $Na_4Ti_3O_7$ would occupy 2*e* Wyckoff sites in octahedral coordination, forming a distorted rock-salt structure with a volume expansion of 6% (Fig. 9). A similar phenomenon is also revealed by Meng et al. [61]. The self-relaxation behavior for the fully intercalated phase is proposed, leading to

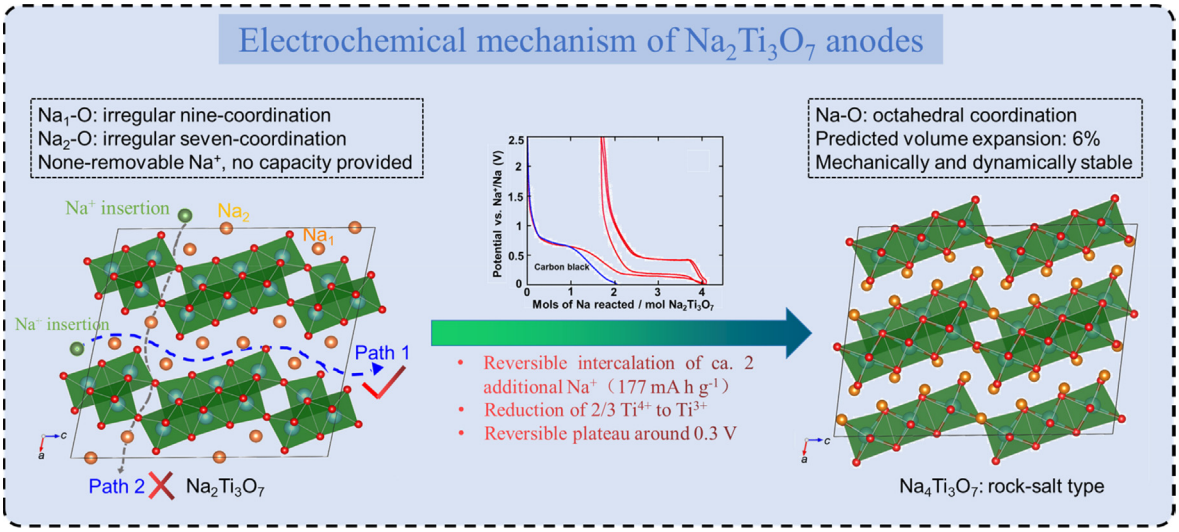


Fig. 9. The electrochemical reaction mechanism of $Na_2Ti_3O_7$ anodes for Na^+ storage.

the self-discharge process [61]. According to Palacín et al., the structure of $Na_4Ti_3O_7$ is mechanically and dynamically stable, showing a reversible Na^+ insertion/extraction process, which has no impact on capacity stability [62]. Palacín also found that the pristine $Na_2Ti_3O_7$ was easily partially converted to the $Na_{2-x}H_xTi_3O_7$ phase via the ion-exchange process due to the presence of water during the sample preparation, which corresponds to discharge plateaus of 1.2 V vs. Na^+/Na. The $Na_{2-x}H_xTi_3O_7$ could gradually restore to $Na_2Ti_3O_7$ by exchanging protons with Na^+ from the electrolyte. Thus the hydrogen ion exchange phenomenon is unrelated to the capacity fading.

Balaya et al. proposed a two-phase reaction mechanism for $Na_2Ti_3O_7$ at the first discharge process, corresponding to the $Na_2Ti_3O_7 \rightarrow Na_{3-x}Ti_3O_7$ and $Na_{3-x}Ti_3O_7 \rightarrow Na_4Ti_3O_7$ [63]. The phase transition process of $Na_2Ti_3O_7 \rightarrow Na_{3-x}Ti_3O_7$ occurs at the discharge plateau close to 0.2 V vs. Na^+/Na, but it is an irreversible transition in the subsequent charge process when deeply discharged to 0.01 V vs. Na^+/Na. When the discharged cut-off voltage is limited to around 0.155 V vs. Na^+/Na instead of 0.01 V vs. Na^+/Na, the phase transformation exhibits a reversible reaction between $Na_2Ti_3O_7$ and $Na_{3-x}Ti_3O_7$. More importantly, the pathway of $Na_2Ti_3O_7 \leftrightarrow Na_{3-x}Ti_3O_7$ exhibits very slight polarization due to a lower charging plateau at 0.22 V vs. Na^+/Na.

4.2. Key issues and challenges of $Na_2Ti_3O_7$ anodes

Until 2011, $Na_2Ti_3O_7$ was reported as a promising low-voltage insertion anode material for developing high-energy sodium-ion batteries because the average potential of 0.3 V vs. Na^+/Na is nearly the lowest one among the ever-reported anodes [11]. Unfortunately, to date, the prospects of practical application of this compound have been hindered by some issues (Fig. 10a and b). A theoretic capacity of the $Na_2Ti_3O_7$ is only 177 mA h g^{-1}, lower than that of hard carbon, which is expected to be increased. The CV curves of the first and second cycle are shown in Fig. 10(a) [64]. In the first cycle, the peak at 0.05 and 0.34 V vs. Na^+/Na corresponds to the Na^+ insertion and extraction. While the large shoulder peak in the potential range from 0.9 to 0.5 V and the reduction peak at 0.32 V correspond to the irreversible decomposition reaction of the electrolyte. The irreversible SEI formation results in initial Coulombic efficiency of only about 60%. In the second cycle, upon Na^+ insertion and extraction, a broad hump appears, suggesting the instability of SEI. Every cycle is affected by some irreversible capacity, leading to a global capacity fading of the electrode (Fig. 10b) [64]. The capacity generally fades ~25% from the first cycle over 10 to 25 cycles [62]. Chen et al. reported that the $Na_2Ti_3O_7$ anodes show a capacity attenuation of over 70% after 60 cycles at 0.1 C rate [59]. Besides, the polarization is over 0.2 V with a charge plateau of 0.44 V vs. Na^+/Na when deep discharged to 0.01 V vs. Na^+/Na [64].

In order to gain new insights into the reasons behind the issues, some in-depth research was carried out. The composition and evolution of SEI in $Na_2Ti_3O_7$ are deeply studied utilizing X-ray photoelectron spectroscopy (XPS) and Auger parameter analysis [65]. The electrochemical measurements were performed at a C/10 rate in the potential range of 0.05–1.6 V vs. Na^+/Na, using 1 M $NaClO_4$ in a mixture (1:1) of ethylene carbonate (EC) and propylene carbonate (PC) as the electrolyte [65]. It is found that the SEI formed at the first discharge process was composed of carbonates and semi-carbonates (Na_2CO_3, $NaCO_3R$), fluorides (NaF), chlorides (NaCl), and poly(ethylene oxide)s (PEO) (Fig. 10c). The NaF is associated with the degradation of the polyvinylidene difluoride (PVDF) binder. The SEI is unstable and partially dissolved during charging, resulting in continuous electrolyte degradation. Casas-Cabanas found that small amounts of insulating Na_2CO_3 (possibly from unreacted precursor or surface corrosion) strongly lead to capacity fading [44]. Blaya et al. found that carbon additive in the composite electrode causes irreversibility between 0.7 and 0.2 V vs. Na^+/Na in the first discharge and charge processes [25]. In summary, the low initial Coulombic efficiency and poor cycling performance of $Na_2Ti_3O_7$ could be mainly related to the decomposition of instable SEI layer, the side-reactions from the PVDF degradation and carbon additive, and the existence of insulating Na_2CO_3 [44,62,64,65].

Casas-Cabanas et al. found that the $Na_{2+x}Ti_3O_7$ ($0 \leq x < 1.4$) exhibits insulation and then becomes an electronic conductor after further Na^+ insertion. Significantly, the observed conductivity transition is reversible upon cycling (Fig. 10d), which may be one of the critical factors for the large polarization of the $Na_2Ti_3O_7$ anode during charging and discharging [64]. Other reasons for the polarization need to be further explored. Regarding the limited specific capacity, it is mainly due to the fact that only 2/3 Ti^{4+} (inserting the two additional Na^+, Fig. 10e) is reduced in the $Na_2Ti_3O_7$ structure, and thus reduction of more Ti^{4+} is the key to enhance the specific capacity. Overall, the key challenges in optimizing the electrochemical performance of $Na_2Ti_3O_7$ anode are the lots of side-reactions, instable SEI layer, and the reversible transition of the

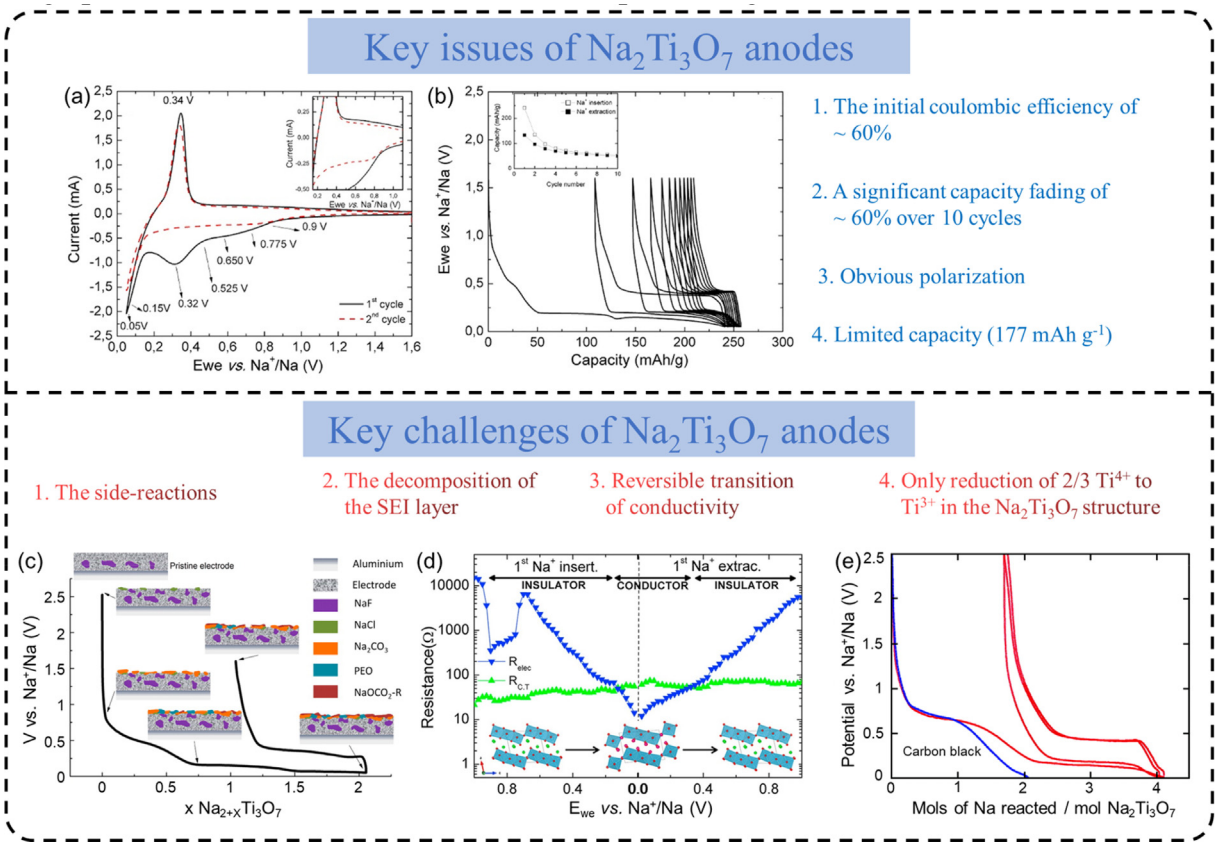


Fig. 10. The key issues and challenges of $Na_2Ti_3O_7$ anodes for Na^+ storage.

conductivity during charging and discharging. There is still some lack of intuitive evidence for the effect of the intrinsic crystal structure on the electrochemical performance of the $Na_2Ti_3O_7$ anode. For an in-depth and comprehensive understanding of the underlying reaction mechanism, some advanced in-situ techniques should be applied [66,67].

4.3. Strategies for optimizing electrochemical performance

As summarized above, $Na_2Ti_3O_7$ still faces many challenges in achieving high-energy and high-safety NIB. Many optimization strategies are proposed. Table S6 summarizes the typical $Na_2Ti_3O_7$-based anode materials and their optimized electrochemical properties for sodium-ion storage [12,25,48,49,51,55,57–59,68–81]. There are four main types of optimization strategies (Fig. 11). The first strategy is the parameters regulation on $Na_2Ti_3O_7$ electrode preparation and electrochemical test, mainly including synthesis parameters, the effect of ball milling, and the types of electrolyte and binder. The second strategy is to composite $Na_2Ti_3O_7$ with carbons, such as carbon-coated $Na_2Ti_3O_7$ materials and $Na_2Ti_3O_7$ composited with N-doped carbon, rGO, and CNT. The third strategy is morphological regulation, such as nanotubes, microspheres, nanoplatelet/nanosheet, and sandwich structures. The fourth strategy is defects regulation of $Na_2Ti_3O_7$ crystal structure including ion substitution, hydrogenated, sulfidation, and new phases for $Na_2Ti_3O_7$ materials. These four optimization strategies are discussed in detail below.

(1) The electrode preparation technologies and electrochemical test conditions are first explored and optimized. It is found that the PVDF binder could react with sodium from electrolytes forming NaF, so this binder should be avoided

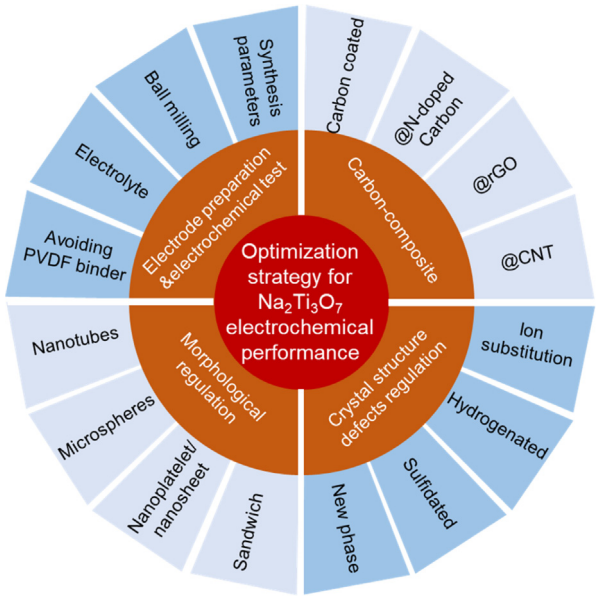
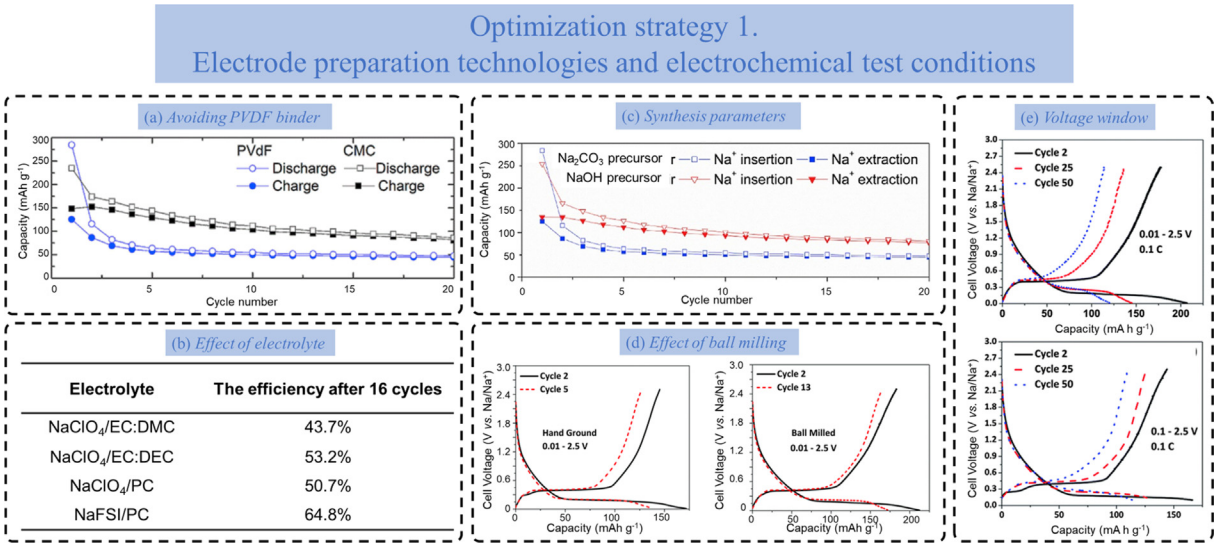


Fig. 11. The optimization strategy of $Na_2Ti_3O_7$ anode materials for sodium-ion batteries.

[65]. The $Na_2Ti_3O_7$ electrode prepared using a carboxymethyl cellulose (CMC) binder performs better than that with PVDF binder (Fig. 12a) [82]. Hu et al. found that $Na_2Ti_3O_7$ exhibits higher capacity and slower capacity decay in 1 M NaFSI/PC with sodium alginate (NaAlg) binder than ones in other electrolytes (including $NaClO_4$/EC:DMC,



Electrolyte	The efficiency after 16 cycles
$NaClO_4$/EC:DMC	43.7%
$NaClO_4$/EC:DEC	53.2%
$NaClO_4$/PC	50.7%
NaFSI/PC	64.8%

Fig. 12. The parameters regulation strategy about $Na_2Ti_3O_7$ electrode preparation and electrochemical test. (a) Capacity evolution of the first 20 cycles of $Na_2Ti_3O_7$ at 17.8 mA g^{-1} in the voltage window 0.05–1.6 V vs. Na^+/Na using PVDF (blue) or CMC (black) as binder. Reproduced with permission from Ref. [82]. Copyright 2016, Elsevier. (b) The effect of the electrolytes on the cyclic performance of $Na_2Ti_3O_7$ electrode employing PVDF as the binder at a current rate of 0.1 C. Reproduced with permission from Ref. [59]. Copyright 2013, Wiley-VCH. (c) Cycling performance at 0.2 C rate of active material hand ground or ball-milled with carbon black. Reproduced with permission from Ref. [25]. Copyright 2013, Royal Society of Chemistry. (d) Na insertion and extraction capacity vs. cycle number at 0.1 C in the voltage window of 0.05–1.6 V vs. Na^+/Na for $Na_2Ti_3O_7$ synthesized by Na_2CO_3 precursor (blue) and NaOH precursor (red). Reproduced with permission from Ref. [44]. Copyright 2015, Elsevier. (e) The effect of voltage window on cycling performance. Reproduced with permission from Ref. [25]. Copyright 2013, Royal Society of Chemistry.

$NaClO_4$/EC:DEC, $NaClO_4$/PC, and NaFSI/PC) (Fig. 12b) [59]. Casas-Cabanas et al. avoided the impurity of Na_2CO_3 in the $Na_2Ti_3O_7$ electrode by eluding the Na_2CO_3 precursor and preventing hydration of $Na_2Ti_3O_7$, efficiently enhancing the capacity retention during the cycling process (Fig. 12c) [44]. Balaya shows a comparison of the $Na_2Ti_3O_7$ electrode prepared by hand-grinding or ball-milling with carbon black. The ball-milled technology could reduce the particle size from 1–2 μm to less than 100 nm, promoting Na^+ diffusion into the bulk, showing a better specific capacity for $Na_2Ti_3O_7$ (Fig. 12d) [25]. The effect of potential range on electrochemical performance was also reported. In the potential range of 0.01–2.5 V vs. Na^+/Na, $Na_2Ti_3O_7$ exhibits a discharge plateau of 0.2 V vs. Na^+/Na and a charge plateau of 0.4 V vs. Na^+/Na. When a lower cut-off potential increases to 0.1 V vs. Na^+/Na, the cycling stability improves significantly, and a new charge plateau at 0.25 V vs. Na^+/Na arises (Fig. 12e) [25]. The new plateau could be related to a reversible pathway of $Na_2Ti_3O_7 \leftrightarrow Na_{3-x}Ti_3O_7$, as mentioned in the part of the reaction mechanism [63].

(2) The strategy of carbon composite is applied to optimize sodium ion storage performance for $Na_2Ti_3O_7$. The carbon layers, CNTs, and reduced graphene oxide (rGO) could enhance electronic conductivity, further decreasing the charge transfer resistance of $Na_2Ti_3O_7$ anodes. Meng et al. reported carbon-coated $Na_2Ti_3O_7$ (Fig. 13a), enhancing the cycling performance (the capacity retention of 65% after 100 cycles) and initial Columbic efficiency (increased by 11% compared to the bare $Na_2Ti_3O_7$) [61]. Casas-Cabanas et al. investigated that the carbon-coated $Na_2Ti_3O_7$ sample could enhance the electrochemical properties. After 100 cycles, the best capacity retention is 78%, with a measured capacity of 124 mA h g^{-1} [44]. $Na_2Ti_3O_7$ hollow spheres assembled from N-doped carbon coated (NTO@N-doped carbon) ultrathin nanosheets were synthesized by Qiao et al., showing an excellent rate capacity of 63 mA h g^{-1} at the current rate of 50 C (Fig. 13b) [73]. Three-dimension reduced graphene oxide (rGO) can provide an ideal conductive matrix for electron/ion transportation, which is applied to optimize the electrochemical performance of $Na_2Ti_3O_7$ materials. Tang et al. reported $Na_2Ti_3O_7$ nanowires embedded in rGO networks (NTO/rGO) as an anode for SIBs. The NTO/rGO delivers a good rate capacity of 116 mA h g^{-1} even at 2 A g^{-1} (Fig. 13c) [48]. Zhang et al. found that one-dimension carbon nanotubes (1D CNTs) can enhance the electronic conductivity of $Na_2Ti_3O_7$/CNTs materials [51]. The $Na_2Ti_3O_7$ in-situ growing on 1D CNTs (NTO@CNT) anode presents an enhanced rate capacity of 100 mA h g^{-1} at the current density of 3.4 A g^{-1} (Fig. 13d).

(3) The strategy of morphology regulation in $Na_2Ti_3O_7$ materials could also effectively optimize the electrochemical performance. Chen et al. found that reducing the particle size of $Na_2Ti_3O_7$ from 5 μm to 140–200 nm could shorten the transport length for Na^+ ions and electrons [59]. During the charging process, the nanosized $Na_2Ti_3O_7$ anode could avoid the appearance of the intermediate phase, enhancing the sodium-ion storage capacity. The $Na_2Ti_3O_7$ with nanotube-like morphology (NTO nanotubes) allows more Na^+ ions (3.5Na^+ per formula unit) to insert/extract in the nanotubes (Fig. 14a), and the reversible discharge capacity is more than 250 mA h g^{-1} with a first Coulombic efficiency below 50%, which is much higher than the reported theoretical capacity of 177 mA h g^{-1} [68]. The theoretical capacity of 311 mA h g^{-1} is predicted, which is proved by observing the appearance of Ti^{3+} and Ti^{2+} after discharging. Li et al. synthesized micros spherical $Na_2Ti_3O_7$ by spray-drying method [54]. The porous microspherical $Na_2Ti_3O_7$ consists of well-crystallized $Na_2Ti_3O_7$ primary particles with a size of 10–20 nm (Fig. 14b). It was found that smaller primary nanoparticles and the porous channels inside the microsphere can reduce the electrochemical polarization and increase the actual electrochemical reaction area, improving electrochemical performance. The microspherical $Na_2Ti_3O_7$ shows a better rate performance, with a capacity of 93.1 mA h g^{-1} at 5 C (72.2 mA h g^{-1} for $Na_2Ti_3O_7$ synthesized by conventional solid-state reaction).

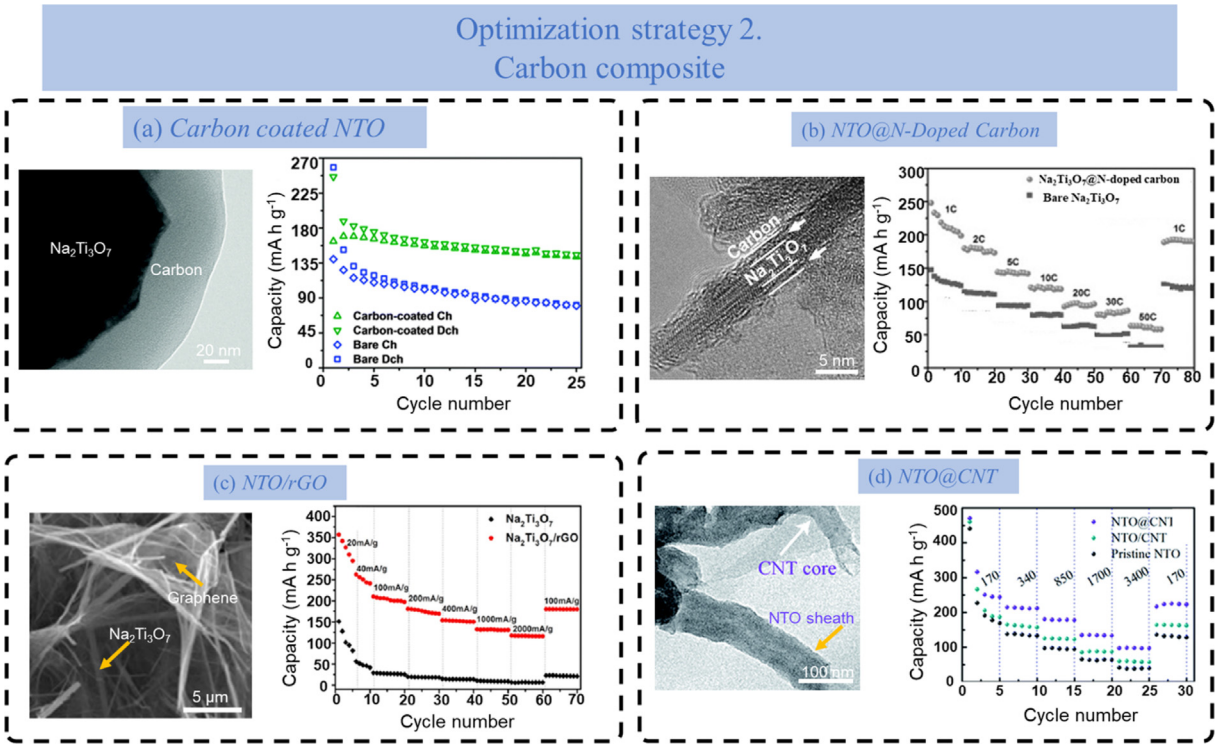


Fig. 13. The carbon-composited strategy. (a) TEM image for carbon-coated NTO and cycling performance of carbon-coated and bare $Na_2Ti_3O_7$. Reproduced with permission from Ref. [61]. Copyright 2014, Royal Society of Chemistry. (b) HRTEM image of NTO@N-doped carbon and the rate performance of NTO@N-doped carbon and bare $Na_2Ti_3O_7$. Reproduced with permission from Ref. [73]. Copyright 2017, Wiley-VCH. (c) SEM image of NTO/rGO and the rate capability of bare $Na_2Ti_3O_7$ and NTO/rGO composite at current densities from 20 mA g^{-1} to 2 A g^{-1} over the voltage window of 0.01–2.5 V vs. Na^+/Na. Reproduced with permission from Ref. [48]. Copyright 2016, Elsevier. (d) TEM image of NTO@CNT and the rate performance from 1.7 to 3.4 A g^{-1} of NTO@CNT, NTO/CNTs, and pristine NTO. Reproduced with permission from Ref. [51]. Copyright 2015, Royal Society of Chemistry.

Dunn et al. synthesized $Na_2Ti_3O_7$ nanoplatelets and nanosheets [53]. The 2D nanoscale morphologies were found to overcome the limitation of charge transfer during Na^+-storage. The mixture morphology of nanoplatelets and nanosheets exhibits far better Na^+-storage capacity (110 mA h g^{-1} at 10 C) and stable cycling behavior than the corresponding bulk materials (Fig. 14c). Qiao et al. designed the $Na_2Ti_3O_7$ nanosheets sandwiched between graphene layers (NTO/rGO sandwich) [75]. The ultrathin $Na_2Ti_3O_7$ nanosheets could reduce the diffusion distance while the rGO layers enhance conductivity. The NTO/rGO sandwich delivers the excellent cycling stability (72 mA h g^{-1} at 5 A g^{-1} after 10,000 cycles) and rate performance (97 mA h g^{-1} at 5 A g^{-1}, Fig. 14d). Besides, the flexible sandwiched structure is a good candidate for flexible sodium-ion batteries. Based on the nanostructures reported so far, the nanotube morphology for $Na_2Ti_3O_7$ is beneficial to obtain superior specific capacity, while the $Na_2Ti_3O_7$ nanoplatelet morphology has an advantage of obtaining superior rate performance.

(4) The strategy of crystal structure regulation is used for electrochemical optimization. The surface-engineered strategies are investigated by Li et al. [58,70]. The hydrogenated $Na_2Ti_3O_7$ nanoarrays with electrical conductivity of 1.2×10^{-4} S cm^{-1} exhibits higher carrier density for Na^+ storage due to the increased oxygen vacancy by hydrogenation (Fig. 15a) [58]. Owing to the optimized conductivity and nanoarrays structures, the hydrogenated $Na_2Ti_3O_7$ anode exhibits marked redox peaks at 0.25/0.65 V vs. Na^+/Na and desirable reversible capacity (227 mA h g^{-1}). The surface-engineered strategies through the sulfidation process are also reported, which exhibit a high electrochemical activity (Fig. 15b) [70]. The $Na_2Ti_3O_7$ with sulfation strategy delivers higher specific capacity compared to hydrogenated strategy. As described in the part of physical property, the conductivity of $Na_2Ti_3O_7$ could be improved by ion doping. Based on the ion-exchange properties of $Na_2Ti_3O_7$, the optimized strategy of the partial replacement of Na^+ ions by other ions was reported. There is some research on $Na_{2-x}H_xTi_3O_7$ for Na^+ ions storage [31,82–84]. Casas-Cabanas et al. investigated the moisture and stability of $Na_2Ti_3O_7$ anodes [82]. The spontaneous Na^+/H^+ exchange could occur after air exposure, forming $Na_{2-x}H_xTi_3O_7$. However, spontaneous Na^+/H^+ exchange only affects the electrochemical behavior of the first cycle (additional plateau of 1.25 V vs. Na^+/Na related to the H^+ ions) (Fig. 15c).

Yu et al. reported the influence of Ti/V cation exchange (forming $Na_2Ti_{3-x}V_xO_7$) in $Na_2Ti_3O_7$ on electrochemical performance based on a first-principles study [85]. The specific capacity could increase from 177 mA h g^{-1} in $Na_2Ti_3O_7$ to over 280 mA h g^{-1} in $Na_2Ti_{3-x}V_xO_7$ due to a higher oxidation state of V^{5+}. Besides, lower voltage, small volume expansion rates below 3%, and a noticeable improvement in electronic transport are presented (Fig. 15d). Wong et al. evaluated the electrochemical performance of the Nb-doped $Na_2Ti_3O_7$ ($Na_2Ti_{2.97}Nb_{0.03}O_7$) [86]. $Na_2Ti_{2.97}Nb_{0.03}O_7$ shows lower electrochemical polarization due to faster charge transport and better electrochemical performances. Mei et al. proposed that engineering of oxygen vacancies and Bi substitution ($Bi_xNa_{2-x}Ti_3O_y$, $0 < x < 2$, $0 < y < 7$) could open fast ion transport channels in three-dimensional within the intrinsic $Na_2Ti_3O_7$ frameworks (Fig. 15e) [80]. $Bi_xNa_{2-x}Ti_3O_y$ anode presents the enhanced reversible capacity (~145% enhancement at 20 mA h g^{-1}), the rate capability (~200% enhancement at 500 mA h g^{-1}), and the cycling stability (~210% enhancement of retention capacity after 150 cycles at 20 mA h g^{-1}) compared with $Na_2Ti_3O_7$. Other ions-doped $Na_2Ti_3O_7$ materials are also reported, including Ti^{3+}-doped

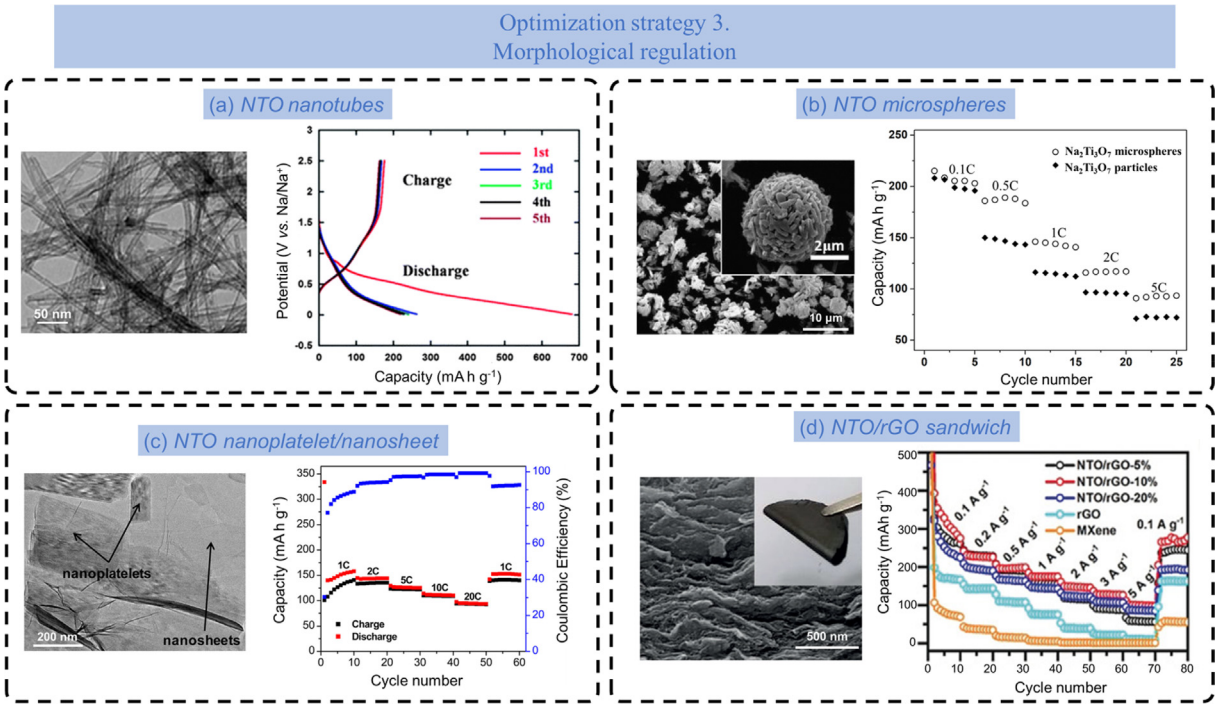


Fig. 14. The morphological regulation strategy. (a) TEM image of the NTO nanotubes and the initial five charge and discharge curves at a current density of 354 mA g^{-1} between 0.01 and 2.5 V vs. Na^+/Na. Reproduced with permission from Ref. [68]. Copyright 2013, Royal Society of Chemistry. (b) SEM image of NTO microspheres and the rate performances of NTO microspheres and NTO particles in the rate of 0.1, 0.5, 1, 2, and 5 C in a voltage window of 0.05–2.0 V vs. Na^+/Na. Reproduced with permission from Ref. [54]. Copyright 2013, Elsevier. (c) TEM image of NTO nanoplatelets/nanosheets and the capacity and Coulombic efficiency measured from galvanostatic cycling at current densities between 100 and 2000 mA cm^{-2} (1 C is estimated as 100 mA cm^{-2}). Reproduced with permission from Ref. [53]. Copyright 2016, American Chemical Society. (d) Side-view SEM image, digital photograph of NTO/rGO sandwich, and the comparison of rate performance of NTO with different rGO content, rGO and MXene at various current densities. Reproduced with permission from Ref. [75]. Copyright 2018, Wiley-VCH.

[76], Yb-doped [77], and P-doped [78]. Li et al. found that the $Na_2Ti_3O_7$ materials in different phase structures could show similar insertion potentials but different electrochemical stability [12]. A new triclinic phase $Na_2Ti_3O_7$ anode delivers a capacity retention of 94.7% (far exceeding the 25.7% of the monoclinic $Na_2Ti_3O_7$), while keeping the low average potential of 0.3 V vs. Na^+/Na similar to that in monoclinic $Na_2Ti_3O_7$. The enhancement is possibly related to smoother Na^+ transport channels and a more stable layered structure with minor fluctuation (Fig. 15f).

Overall, these four strategies show a synergistic effect on performance improvement of $Na_2Ti_3O_7$ anodes. Avoiding the use of PVDF binder, developing new electrolyte and conductive additives, reducing particle size, avoiding the appearance of Na_2CO_3, setting the voltage window to 0.1–3 V vs. Na^+/Na, carbon-composite, and Bi doping can effectively enhance the initial Coulombic efficiency and cycling stability of $Na_2Ti_3O_7$ anodes. Carbon composite technology is mainly used to optimize the rate performance and has no obvious advantage in reducing polarization. In order to decrease the degree of polarization, reducing the particle size of $Na_2Ti_3O_7$ materials, creating more sodium ion transport channels, and Nb doping are more effective strategies. The strategies for enhancing the capacity include the use of $Na_2Ti_3O_7$ nanotubes, reducing the particle size, hydrogenated or sulfation strategies, and introducing high oxidation state of V^{5+}.

4.4. The applications of $Na_2Ti_3O_7$ in sodium-ion full cells

The advantages of $Na_2Ti_3O_7$ as low-voltage insertion anode material are evaluated by assembling a sodium-ion full cell. Meng et al. design a $Na_2Ti_3O_7$//P2-$Na_{0.8}Li_{0.12}Ni_{0.22}Mn_{0.66}O_2$ full cell, which displays a high average voltage of 3.1 V due to the ultralow voltage of $Na_2Ti_3O_7$ anode [61]. The capacity retention after 25 cycles is ~63%, and the overall energy density is 100 Wh kg^{-1}. $Na_{2/3}(Ni_{1/3}Mn_{2/3})O_2$ materials are promising cathodes for sodium-ion storage. A full cell by matching hydrogenated $Na_2Ti_3O_7$ (denoted as H-$Na_2Ti_3O_7$) anodes with $Na_{2/3}(Ni_{1/3}Mn_{2/3})O_2$ cathodes afford a reversible capacity of 53 mA h g^{-1} (based on the total mass of both electrodes), with an average cell voltage of 2.7 V [58]. In a working voltage range of 2.0–3.2 V, $Na_2Ti_3O_7$ nanotube//$Na_{2/3}(Ni_{1/3}Mn_{2/3})O_2$ delivers a specific energy of 110 Wh kg^{-1} [70]. The $VOPO_4$ materials are also chosen as cathodes. The $Na_2Ti_3O_7$//$VOPO_4$ full cells display a capacity retention of 92.4% after 100 cycles and an energy density of 220 Wh kg^{-1} (Fig. 16) [49]. Moreover, the temperature-dependent charge–discharge tests indicate excellent capacity retention of 128% and about 60% at 55 and −20 °C, respectively [49].

Activated carbon (AC) cathode with an electric double-layer mechanism is applied. The assembled $Na_2Ti_3O_7$@CNT//AC full cell delivers an energy density of 58.5 Wh kg^{-1}, a power density of 3 kW kg^{-1}, and a capacity retention of 75% after 4000 cycles (Fig. 16) [51]. Zhang et al. extend the application of $Na_2Ti_3O_7$ to 3D flexible sodium-ion batteries [57], based on 3D-flexible $Na_2Ti_3O_7$ nanosheet arrays/carbon textiles (denoted NTO/CT) as anode and flexible reduced graphene oxide film (GFs) as cathode without metal current collector or conducting additives. The flexible NTO/CT//GFs full cell achieves an energy density of 55 Wh kg^{-1} and a power density of 3 kW kg^{-1} (Fig. 16) [57]. $Na_2Ti_3O_7$ anodes are also applied to quasi-solid-state sodium-ion capacitors. Matching with peanut shell derived carbon (PSC) cathode, the assembled $Na_2Ti_3O_7$//PSC full cell displays an energy density of 111.2 Wh kg^{-1} at a power density of 800 W kg^{-1}, and a capacity retention of 86% after 3000 cycles (Fig. 16) [69]. A quasi-solid-state Na-ion full cell, based

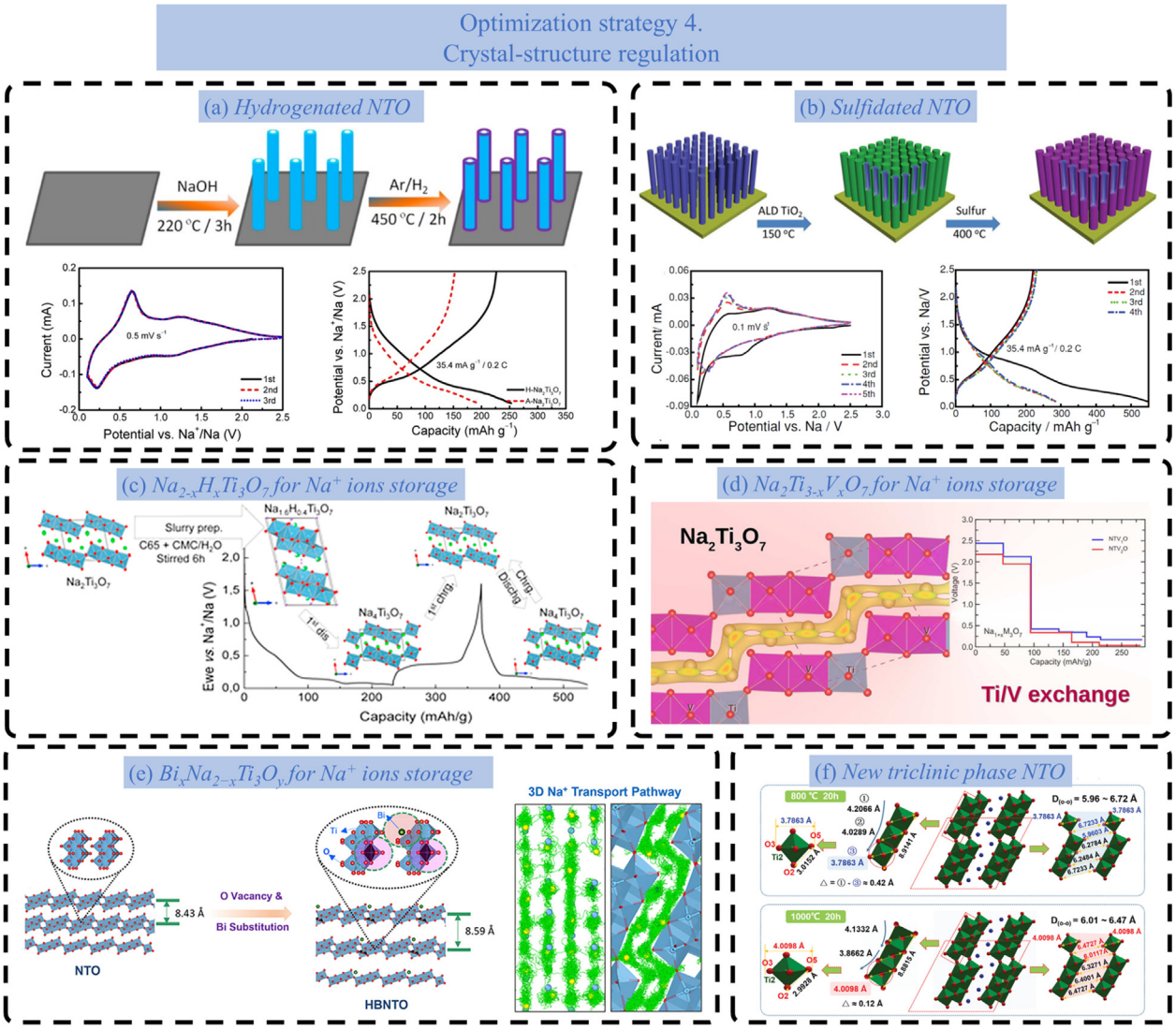


Fig. 15. The crystal-structure regulation strategy. (a, b) Schematic illustration of a fabrication process of hydrogenated NTO nanoarrays and sulfidated NTO nanotube grown on Ti foil and the relevant CV and charge/discharge curves. Reproduced with permission from Ref. [58,70]. Copyright 2016, American Chemical Society, Copyright 2016, Wiley-VCH. (c) The crystal structure evolution of $Na_{2-x}H_xTi_3O_7$ during the charge/discharge process. Reproduced with permission from Ref. [82]. Copyright 2016, Elsevier. (d) Na^+ ions migration schematic and voltage vs. capacity curves of $Na_2Ti_{3-x}V_xO_7$. Reproduced with permission from Ref. [85]. Copyright 2020, American Chemical Society. (e) The schematics of engineering of oxygen vacancies and Bi substitution, and three-dimensional fast ion transport channels. Reproduced with permission from Ref. [80]. Copyright 2021, American Chemical Society. (f) The refinement structure of monoclinic and triclinic $Na_2Ti_3O_7$. Reproduced with permission from Ref. [12]. Copyright 2020, Wiley-VCH.

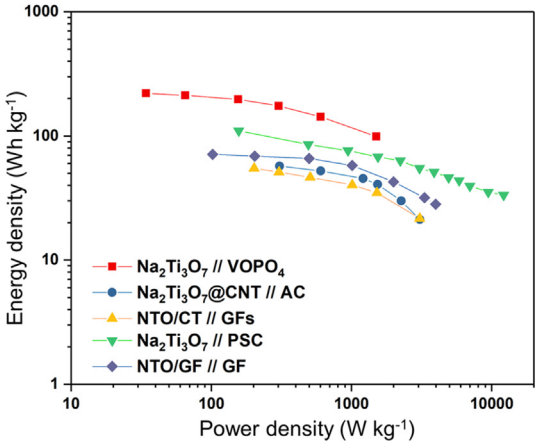


Fig. 16. The energy and power density of the typical sodium-ion full cells using $Na_2Ti_3O_7$ as anode.

on $Na_2Ti_3O_7$ nanoribbon array/graphene foam (NTO/GF) anode and graphene foam (GF) cathode, achieves a high energy of 70.6 Wh kg^{-1} and a power density of 4 kW kg^{-1} [87].

The energy and power density of the typical sodium-ion full cells using $Na_2Ti_3O_7$ as anode are summarized in Fig. 16. It shows that NIBs assembled based on $Na_2Ti_3O_7$ anodes are still far from practical applications despite showing better electrochemical performance. This may be related to many factors, such as cathode materials, test conditions, assembly process, etc. However, solving the critical challenges faced by $Na_2Ti_3O_7$ anodes is an essential step to achieve high-energy and high-safety NIBs.

5. Conclusions and outlooks

This review provides a comprehensive overview of the achievements of $Na_2Ti_3O_7$ materials which is considered as an important anode for obtaining high-energy and high-safety NIBs. Through this review, we can conclude that (1) the layered $Na_2Ti_3O_7$ anodes

display a safe average potential of 0.3 V vs. Na^+/Na and an ability to reversibly insert $2Na^+$ per formula, corresponding to a theory capacity of 177 mA h g^{-1} and a reduction of 2/3 of Ti^{4+} to Ti^{3+}; (2) the sodium-ion storage process of $Na_2Ti_3O_7$ anodes exhibits a phase transformation mechanism, and the Na sublattice would rearrange; (3) the poor cycling performance, obvious polarization and the limited capacity of $Na_2Ti_3O_7$ could be mainly related to the side-reactions and the SEI instability; (4) the unsatisfied rate performance and clear polarization could be mainly related to the poor conductivity of $Na_2Ti_3O_7$ and the insulator behavior of $Na_{2+x}Ti_3O_7$ ($0 \leq x < 1.4$); (5) optimization strategies for electrochemical performance are categorized in four aspects, which show a synergistic effect on the performance improvement of $Na_2Ti_3O_7$ anodes.

Although the reported optimization strategies have improved the electrochemical performance of $Na_2Ti_3O_7$ anodes, these issues of low initial Columbic efficiency, high polarization, unsatisfied cycling stability, and limited capacity are not eliminated. More critically, the low-voltage plateau of many optimized $Na_2Ti_3O_7$ anodes disappears, meaning that the crucial important advantage of the material is lost despite the enhancement of its other electrochemical properties. Based on the above issues, we propose the following potentially meaningful research directions. (1) Deepen the understanding of plateau-composition-property-performance relationships. $Na_2Ti_3O_7$ anodes exhibit a flat discharge voltage of 0.2 V vs. Na^+/Na, significantly lower than other titanium-based anodes (0.5–1 V vs. Na^+/Na) operating with the same Ti^{4+}/Ti^{3+} redox couple. The problem "What affects the redox potential of the Ti^{4+}/Ti^{3+} couple?" would inspire researchers to conduct some basic research. (2) Clarify the relationships between the decay of the voltage plateau and the crystal structure of the $Na_2Ti_3O_7$ material. Why does the plateau of the $Na_2Ti_3O_7$ anodes decay significantly during cycling? Addressing this fundamental question may help to optimize its performance further. (3) Combine the intrinsic properties of $Na_2Ti_3O_7$ materials to optimize their performance. Different materials have different properties, and their uniqueness should be emphasized to propose effective modification strategies. For example, based on the unique ion-exchange properties of the $Na_2Ti_3O_7$, we are investigating several attractive and easy optimization strategies and have so far found significant optimization for cycling stability. (4) Obtain stable SEI layers and reduce the irreversible consumption of Na^+. This is closely related to the cycling stability and initial Coulombic efficiency of $Na_2Ti_3O_7$ anodes. For this purpose, novel electrolytes and conductive additives can be investigated. (5) Reduce the polarization of $Na_2Ti_3O_7$ anode. Currently, there are fewer studies in this area, and it is of great significance to understand the causes of polarization and propose effective optimization strategies. (6) Improve the reversible capacity of the material. The theoretical capacity of $Na_2Ti_3O_7$ anode has been predicted to be as high as 311 mA h g^{-1}, but the experimental results have not yet reached this level. The key is to increase the reduction amount of Ti^{4+} to a lower valence Ti^{2+}, and introduce elements with high electrochemical activity.

Declaration of competing interest

The authors declare that they have no known competing financial interests or personal relationships that could have appeared to influence the work reported in this paper.

Acknowledgments

This work is supported by the National Natural Science Foundation of China (52307239, 52102300, 52207234), the Natural Science Foundation of Hubei Province (2022CFB1003, 2021CFA025).

Appendix A. Supplementary material

Supplementary data to this article can be found online at https://doi.org/10.1016/j.jechem.2023.09.039.

References

[1] M.M. Thackeray, K. Amine, Nat. Energy 6 (2021) 683.
[2] K. Geng, M. Yang, J. Meng, L. Zhou, Y. Wang, S. Dmytro, Q. Zhang, S. Zhong, Q. Ma, Tungsten 4 (2022) 323–335.
[3] T.M. Gür, Energ. Environ. Sci. 11 (2018) 2696–2767.
[4] Y.R. Pei, M. Zhao, Y.P. Zhu, C.C. Yang, Q. Jiang, Nano Mater. Sci. 4 (2022) 104–112.
[5] F. Xiong, Y. Jiang, L. Cheng, R. Yu, S. Tan, C. Tang, C. Zuo, Q. An, Y. Zhao, J.J. Gaumet, L. Mai, Interdiscipl. Mater. 1 (2022) 140–147.
[6] J. Jiang, J. Liu, Interdiscipl. Mater. 1 (2022) 116–139.
[7] S. Guo, J. Yi, Y. Sun, H. Zhou, Energ. Environ. Sci. 9 (2016) 2978–3006.
[8] N. Tapia-Ruiz, A.R. Armstrong, H. Alptekin, M.A. Amores, H. Au, J. Barker, R. Boston, W.R. Brant, J.M. Brittain, Y. Chen, M. Chhowalla, Y.-S. Choi, S.I.R. Costa, M. Crespo Ribadeneyra, S.A. Cussen, E.J. Cussen, W.I.F. David, A.V. Desai, S.A.M. Dickson, E.I. Eweka, J.D. Forero-Saboya, C.P. Grey, J.M. Griffin, P. Gross, X. Hua, J. T.S. Irvine, P. Johansson, M.O. Jones, M. Karlsmo, E. Kendrick, E. Kim, O.V. Kolosov, Z. Li, S.F.L. Mertens, R. Mogensen, L. Monconduit, R.E. Morris, A.J. Naylor, S. Nikman, C.A. O'Keefe, D.M.C. Ould, R.G. Palgrave, P. Poizot, A. Ponrouch, S. Renault, E.M. Reynolds, A. Rudola, R. Sayers, D.O. Scanlon, S. Sen, V.R. Seymour, B. Silván, M.T. Sougrati, L. Stievano, G.S. Stone, C.I. Thomas, M.-M. Titirici, J. Tong, T.J. Wood, D.S. Wright, R. Younesi, J. Phys.: Energy 3 (2021) 031503.
[9] J.M. Tarascon, Joule. 4 (2020) 1616–1620.
[10] M. Patel, K. Mishra, R. Banerjee, J. Chaudhari, D.K. Kanchan, D. Kumar, J. Energy Chem. 81 (2023) 221–259.
[11] P. Senguttuvan, G. Rousse, V. Seznec, J.M. Tarascon, M.R. Palacín, Chem. Mater. 23 (2011) 4109–4111.
[12] Y. Cao, Q. Ye, F. Wang, X. Fan, L. Hu, F. Wang, T. Zhai, H. Li, Adv. Funct. Mater. 30 (2020) 2003733.
[13] D. Chen, W. Zhang, K. Luo, Y. Song, Y. Zhong, Y. Liu, G. Wang, B. Zhong, Z. Wu, X. Guo, Energ. Environ. Sci. 14 (2021) 2244–2262.
[14] H. Zhai, B.Y. Xia, H.S. Park, J. Mater. Chem. A 7 (2019) 22163–22188.
[15] D. Lv, D. Wang, N. Wang, H. Liu, S. Zhang, Y. Zhu, K. Song, J. Yang, Y. Qian, J. Energy Chem. 68 (2022) 104–112.
[16] T. Li, L. Kong, X. Bai, Y. Wang, Y. Qi, J. Energy Chem. 81 (2023) 379–388.
[17] J. Dong, Y. Jiang, Q. Li, Q. Wei, W. Yang, S. Tan, X. Xu, Q. An, L. Mai, J. Mater. Chem. A 5 (2017) 10827–10835.
[18] J. Dong, Y. He, Y. Jiang, S. Tan, Q. Wei, F. Xiong, Z. Chu, Q. An, L. Mai, Nano Energy 73 (2020) 104838.
[19] S. Tan, Y. Jiang, Q. Wei, Q. Huang, Y. Dai, F. Xiong, Q. Li, Q. An, X. Xu, Z. Zhu, X. Bai, L. Mai, Adv. Mater. 30 (2018) e1707122.
[20] Y. Jiang, Y. Shen, J. Dong, S. Tan, Q. Wei, F. Xiong, Q. Li, X. Liao, Z. Liu, Q. An, L. Mai, Adv. Energy Mater. 9 (2019) 1900967.
[21] Y. Jiang, J. Dong, S. Tan, Q. Wei, F. Xiong, W. Yang, Y. Shen, Q. Zhang, Z.A. Liu, Q. An, L. Mai, J. Energy Chem. 55 (2021) 295–303.
[22] Y. Jiang, H. Wang, J. Dong, Q. Zhang, S. Tan, F. Xiong, W. Yang, S. Zhu, Y. Shen, Q. Wei, Q. An, L. Mai, Small 18 (2022) e2200805.
[23] Y. Shen, Y. Jiang, Z. Yang, J. Dong, W. Yang, Q. An, L. Mai, Adv. Sci. 9 (2022) e2104504.
[24] A. Kumar Prajapati, A. Bhatnagar, J. Energy Chem. 83 (2023) 509–540.
[25] A. Rudola, K. Saravanan, C.W. Mason, P. Balaya, J. Mater. Chem. A 1 (2013) 2653.
[26] X. Gu, S. Qiao, X. Ren, X. Liu, Y. He, X. Liu, T. Liu, Rare Met. 40 (2021) 828–836.
[27] X. Qi, Y. Liu, L. Ma, B. Hou, H. Zhang, X. Li, Y. Wang, Y. Hui, R. Wang, C. Bai, H. Liu, J. Song, X. Zhao, Rare Met. 41 (2022) 1637–1646.
[28] S. Andersson, Acta Cryst 14 (1961) 1245–1249.
[29] O.V. Yakubovich, V.V. Kireev, Cryrallography Rep. 48 (2003) 24–28.
[30] A.A. Araújo-Filho, F.L.R. Silva, A. Righi, M.B. da Silva, B.P. Silva, E.W.S. Caetano, V.N. Freire, J. Solid State Chem. 250 (2017) 68–74.
[31] A. Eguia-Barrio, E. Castillo-Martinez, M. Zarrabeitia, M.A. Munoz-Marquez, M. Casas-Cabanas, T. Rojo, Phys. Chem. Chem. Phys. 17 (2015) 6988–6994.
[32] S. Pal, C. Prem, S.D. Pandey, J. Mater. Sci. Mater. Electron. 2 (1991) 89–93.
[33] D. Pal, R.K. Pal, J.L. Pandey, S.H. Abdi, A.K. Agnihotri, J. Mater. Sci. Mater. Electron. 21 (2010) 1181–1185.
[34] Y. An, Z. Li, H. Xiang, Y. Huang, J. Shen, Eur. J. Phys. 9 (2011) 1488–1492.
[35] H. Irawa, S. Kikkawa, M. Kolzuml, J. Phys. Chem. 86 (1982) 5023–5026.
[36] S. Kikkawa, F. Yasuda, M. Koizumi, Mater. Res. Bull. 20 (1985) 1221–1227.
[37] Y.S. Choi, S.I.R. Costa, N. Tapia-Ruiz, D.O. Scanlon, ACS Appl. Energy Mater. 6 (2023) 484–495.
[38] Y. An, D. Wang, C. Wu, Physica E 60 (2014) 210–213.
[39] N. Miyamoto, K. Kuroda, M. Ogawa, J. Mater. Chem. 14 (2004) 165.
[40] J. Yang, D. Li, X. Wang, X. Yang, L. Lu, J. Mater. Sci. 38 (2003) 2907–2911.
[41] K. Chiba, N. Kijima, Y. Takahashi, Y. Idemoto, J. Akimoto, Solid State Ion. 178 (2008) 1725–1730.
[42] M. Vithal, S. Rama Krishna, G. Ravi, S. Palla, R. Velchuri, S. Pola, Ceram. Int. 39 (2013) 8429–8439.
[43] C.K. Ho, C.Y.V. Li, K.Y. Chan, Ind. Eng. Chem. Res. 55 (2016) 10065–10072.

[44] M. Zarrabeitia, E. Castillo-Martínez, J.M. López Del Amo, A. Eguía-Barrio, M.Á. Muñoz-Márquez, T. Rojo, M. Casas-Cabanas, Acta Mater. 104 (2016) 125–130.
[45] M. Xie, K. Wang, R. Chen, L. Li, F. Wu, Chem. Res. Chin. Univ. 31 (2015) 443–446.
[46] Z. Yan, L. Liu, H. Shu, X. Yang, H. Wang, J. Tan, Q. Zhou, Z. Huang, X. Wang, J. Power Sources 274 (2015) 8–14.
[47] C. Piffet, B. Vertruyen, F. Hatert, R. Cloots, F. Boschini, A. Mahmoud, J. Energy Chem. 65 (2022) 210–218.
[48] Z. Zhou, H. Xiao, F. Zhang, X. Zhang, Y. Tang, Electrochim. Acta 211 (2016) 430–436.
[49] H. Li, L. Peng, Y. Zhu, D. Chen, X. Zhang, G. Yu, Energ. Environ. Sci. 9 (2016) 3399–3405.
[50] Q. Du, G. Lu, J. Nanosci. Nanotechnol. 15 (2015) 4385–4391.
[51] S. Dong, L. Shen, H. Li, P. Nie, Y. Zhu, Q. Sheng, X. Zhang, J. Mater. Chem. A 3 (2015) 21277–21283.
[52] Z. Zhang, J.B. Goodall, S. Brown, L. Karlsson, R.J. Clark, J.L. Hutchison, I.U. Rehman, J.A. Darr, Dalton Trans. 39 (2010) 1488–1492.
[53] J.S. Ko, V.V. Doan-Nguyen, H.S. Kim, G.A. Muller, A.C. Serino, P.S. Weiss, B.S. Dunn, ACS Appl. Mater. Interfaces. 9 (2017) 1416–1425.
[54] W. Zou, J. Li, Q. Deng, J. Xue, X. Dai, A. Zhou, J. Li, Solid State Ion. 262 (2014) 192–196.
[55] S. Anwer, Y. Huang, J. Liu, J. Liu, M. Xu, Z. Wang, R. Chen, J. Zhang, F. Wu, ACS Appl. Mater. Interfaces. 9 (2017) 11669–11677.
[56] S. Chen, Y. Pang, J. Liang, S. Ding, J. Mater. Chem. A 6 (2018) 13164–13170.
[57] S. Dong, L. Shen, H. Li, G. Pang, H. Dou, X. Zhang, Adv. Funct. Mater. 26 (2016) 3703–3710.
[58] S. Fu, J. Ni, Y. Xu, Q. Zhang, L. Li, Nano Lett. 16 (2016) 4544–4551.
[59] H. Pan, X. Lu, X. Yu, Y.S. Hu, H. Li, X.Q. Yang, L. Chen, Adv. Energy Mater. 3 (2013) 1186–1194.
[60] G. Rousse, M.E. Arroyo-de Dompablo, P. Senguttuvan, A. Ponrouch, J.M. Tarascon, M.R. Palacín, Chem. Mater. 25 (2013) 4946–4956.
[61] J. Xu, C. Ma, M. Balasubramanian, Y.S. Meng, Chem. Commun. 50 (2014) 12564–12567.
[62] J. Nava-Avendaño, A. Morales-García, A. Ponrouch, G. Rousse, C. Frontera, P. Senguttuvan, J.M. Tarascon, M.E.A.-d. Dompablo, M.R. Palacín, J. Mater. Chem. A 3 (2015) 22280–22286.
[63] A. Rudola, N. Sharma, P. Balaya, Electrochem. Commun. 61 (2015) 10–13.
[64] M. Zarrabeitia, F. Nobili, M.Á. Muñoz-Márquez, T. Rojo, M. Casas-Cabanas, J. Power Sources 330 (2016) 78–83.
[65] M.A. Munoz-Marquez, M. Zarrabeitia, E. Castillo-Martinez, A. Eguia-Barrio, T. Rojo, M. Casas-Cabanas, ACS Appl. Mater. Interfaces. 7 (2015) 7801–7808.
[66] X. Lin, X. Yang, H. Chen, Y. Deng, W. Chen, J. Dong, Y. Wei, J. Li, J. Energy Chem. 76 (2023) 146–164.
[67] H. Wang, F. Liu, R. Yu, J. Wu, Interdiscipl. Mater. 1 (2022) 196–212.
[68] W. Wang, C. Yu, Z. Lin, J. Hou, H. Zhu, S. Jiao, Nanoscale 5 (2013) 594–599.
[69] H. Li, L. Peng, Y. Zhu, X. Zhang, G. Yu, Nano Lett. 16 (2016) 5938–5943.
[70] J. Ni, S. Fu, C. Wu, Y. Zhao, J. Maier, Y. Yu, L. Li, Adv. Energy Mater. 6 (2016) 1502568.
[71] Y. Ge, J. Zhu, M. Dirican, H. Jia, M. Yanilmaz, Y. Lu, C. Chen, Y. Qiu, X. Zhang, Mater. Lett. 188 (2017) 176–179.
[72] M. Li, X. Xiao, X. Fan, X. Huang, Y. Liu, L. Chen, J. Alloy. Compd. 712 (2017) 365–372.
[73] F. Xie, L. Zhang, D. Su, M. Jaroniec, S.Z. Qiao, Adv. Mater. 29 (2017) 1700989.
[74] R. Bi, C. Zeng, T. Ma, A. Etogo, X. Wang, L. Zhang, Electrochim. Acta 284 (2018) 287–293.
[75] C. Zeng, F. Xie, X. Yang, M. Jaroniec, L. Zhang, S.Z. Qiao, Angew. Chem. Int. Ed. 57 (2018) 8540–8544.
[76] T. Song, S. Ye, H. Liu, Y.-G. Wang, J. Alloy. Compd. 767 (2018) 820–828.
[77] J. Xia, H. Zhao, W.K. Pang, Z. Yin, B. Zhou, G. He, Z. Guo, Y. Du, Chem. Sci. 9 (2018) 3421–3425.
[78] D.S. Liu, F. Jin, A. Huang, X. Sun, H. Su, Y. Yang, Y. Zhang, X. Rui, H. Geng, C.C. Li, Chemistry 25 (2019) 14881–14889.
[79] J. Liu, Z. Wang, Z. Lu, L. Zhang, F. Xie, A. Vasileff, S.Z. Qiao, ACS Mater. Lett. 1 (2019) 389–398.
[80] J. Mei, T. Wang, D. Qi, J. Liu, T. Liao, Y. Yamauchi, Z. Sun, ACS Nano 15 (2021) 13604–13615.
[81] H. Chen, Y. Wu, J. Duan, R. Zhan, W. Wang, M.Q. Wang, Y. Chen, M. Xu, S.J. Bao, ACS Appl. Mater. Interfaces 11 (2019) 42197–42205.
[82] M. Zarrabeitia, E. Castillo-Martínez, J.M. López Del Amo, A. Eguía-Barrio, M.A. Muñoz-Márquez, T. Rojo, M. Casas-Cabanas, J. Power Sources 324 (2016) 378–387.
[83] Y. Xu, D. Bauer, M. Lübke, T.E. Ashton, Y. Zong, J.A. Darr, J. Power Sources 408 (2018) 28–37.
[84] S. Wang, W. Wang, P. Zhan, Y. Yuan, K. Jiao, H. Jiao, S. Jiao, J. Mater. Chem. A 3 (2015) 16528–16534.
[85] C.J. Yu, S.G. Hwang, Y.C. Pak, S.H. Choe, J.S. Kim, K.C. Ri, J. Phys. Chem. C 124 (2020) 17897–17906.
[86] J. Chen, X. Zhou, C. Mei, J. Xu, C. Wong, Electrochim. Acta 224 (2017) 446–451.
[87] S. Dong, L. Wu, J. Wang, P. Nie, H. Dou, X. Zhang, J. Mater. Chem. A 5 (2017) 5806–5812.